Electronic Supplementary Material (ESI) for Catalysis Science & Technology.
This journal is © The Royal Society of Chemistry 2023

Supporting Information

Polyoxometalate (POM) boosting the light-harvesting ability of graphitic carbon nitride for efficient photocatalytic hydrogen production

Simon Yves Djoko T.[1], Estella Njoyim T.[2], Anh Dung Nguyen[1], Jin Yang[3], Hüseyin Küçükkeçeci[3], Edith Mawunya Kutorglo[1], Babu Radhakrishnan[4], Klaus Schwarzburg[4], Shahana Huseyinova[1], Prasenjit Das[3], Yasmine Ziouani[3], Minoo Tasbihi[1], Michael Schwarze[1], Arne Thomas[3], Reinhard Schomäcker[1,*]

[1]Technische Universität Berlin, Department of Chemistry, Multiphase Reaction Engineering, TC8, Straße des 17. Juni 124, 10623 Berlin, Germany
[2]University of Bamenda, Higher Teacher Training College, Department of Chemistry, P.O.Box 39 Bambili, Cameroon
[3]Technische Universität Berlin, Department of Chemistry, Functional materials BA216 Hardenbergstr. 40, 10623 Berlin, Germany
[4]Helmholtz-Zentrum Berlin für Materialien und Energie, Hahn-Meitner-Platz 1, 14109 Berlin

*Corresponding author: Reinhard Schomäcker (schomaecker@tu-berlin.de)

Contents

Section 1: Experimental section 2
Section 2: Additional discussions 6
Figure SI 1: Comparison of SEM images of bulk composites (gCN/PMA$_x$) 6
Figure SI 2: SEM of gCN 7
Figure SI 3: XRD patterns of P-gCN/PMA$_2$, (i) P-gCN/PMA$_{2.5}$ and PMA-450 8
Figure SI 4: XRD patterns gCN/PMA$_{0.1}$, gCN/PMA$_{0.2}$, gCN/PMA$_{0.3}$, gCN/PMA$_{0.4}$ 9
Figure SI 5: FT-IR spectrum of PMA[6,7] 9
Figure SI 6: FT-IR spectra of gCN and P-gCN/PMA$_{0.5}$, gCN/PMA$_{0.2}$, gCN/PMA$_{0.5}$ 10
Figure SI 7: FT-IR spectra of gCN, gCN-450° C, and all P-gCN/PMA$_x$ 10
Table SI 1: Brunauer-Emmett-Teller (BET) Surface Area 12
Figure SI 8: N_2 adsorption-desorption isotherms of as-prepared samples 12
Figure SI 9: Band energy estimation of gCN (a) and P-gCN/PMA$_x$ (b-h). 14
Figure SI 10: UV-vis diffuse absorption spectra 15
Figure SI 11: Direct and indirect band energy estimation of PMA. 16
Figure SI 12: XPS survey spectra, high-resolution XPS spectra 17
Figure SI 13: XPS survey spectra, high-resolution XPS spectra 18
Figure SI 14: XPS survey spectra of P-gCN/PMA$_{2.5}$ catalyst proving the evidence of Mo and P 19
Figure SI 15: Survey and High-resolution deconvoluted XPS spectra 19
Table SI 2: XPS valence band values with VBM and CBM 20
Table SI 3: Elemental composition of samples analyzed from ICP-OES, EDX, XPS, and CEA technique 21
Section 3: Photocatalytic experiments 22

Figure SI 16: Laboratory set up for the photocatalytic HER testing 23
Figure SI 17: Effect of P-gCN/PMA1.5 concentration (a) and effect of temperature (b) 25
Figure SI 19: P-gCN/PMA$_{1.5}$ before and after the photocatalytic reaction 28
Figure SI 20: gCN before and after the photocatalytic reaction 28
Figure SI 21: Photoluminescence (PL) spectra of P-gCN/PMA$_{1.5}$ (a) and gCN (b) 29
Table SI 4: Operating conditions and H_2 evolution from overall water splitting 30
Table SI 22: FWHM of XRD patterns disclosing the crystallinity 31
Figure SI 23: TEM images 31
Figure SI 24: EDX spectroscopy (a) and elemental mapping (b) of gCN 32
Figure SI 25: EDX spectroscopy (a) and elemental mapping (b) of bulk gCN/PMA$_{0.5}$ 33
Figure SI 26: EDX spectroscopy (a) and elemental mapping (b) of P-gCN/PMA$_{0.5}$ 33
Figure SI 27: EDX spectroscopy (a) and elemental mapping (b) of bulk gCN/PMA$_{1.5}$ 34
Figure SI 28: EDX spectroscopy (a) and elemental mapping (b) of P-gCN/PMA$_{1.5}$ 34
Table SI 29: Comparison of hydrogen evolution rates based on CN derivatives 35
Figure SI 30: Comparison of time-resolved transient PL decay spectra of 35
Figure SI 31: XRD patterns of gCN and P-gCN/PMA$_{1.5}$: After (a, b) and before (b, c) 36

Section 1: Experimental section

Chemicals: All chemicals were of analytical and reagent grade (ACS, reagent) from Merk, Sigma-Aldrich, VWR, and Alfa Aesar, and they were used without further purification. Cyanamide (CH_2N_2 - 99%) was obtained from Sigma-Aldrich and used as the precursor of graphitic carbon nitride (gCN). Phosphomolybdic acid hydrate (PMA-$H_3Mo_{12}PO_{40}$•xH_2O) is a POM of Keggin type. It was purchased from Sigma-Aldrich and used as the coupling material to drive the templated doping synthesis giving rise to structured P-doped gCN. A mixture of methanol (MeOH - 99%) purchased from VWR and distilled water (DW) was used as solvent for the solvothermal synthesis of the gCN/PMA composite. 2-propanol (IPA, > 99.8 %) obtained from VWR was used as a cleaning solvent for the purification of bulk-gCN. Triethanolamine (TEOA, 98%) obtained from Merk was used in photocatalytic tests as a sacrificial reagent mixed with hexachloroplatinic acid (H_2PtCl_6) as the co-catalyst precursor obtained from Merk. Milli-Q water (ultrapure water) was used in all photocatalytic experiments to drive HER.

Materials: For the synthesis part, the following lab equipment was used: 50 mL Teflon-lined stainless-steel autoclave supplied by Parr Instrument Company. Ramp programming Muffle furnace from Nabertherm company. Vacuum oven (Vacutherm) from Heraeus. Ceramic milling mortar and ceramic crucible with cover purchased from Alfa Aesar.

Safety & hazards:

When reproducing this experimental work, the following precautions should be considered:

1. The precursor cyanamide is a toxic substance and during the synthesis of graphitic carbon nitride, toxic fumes are produced. The synthesis must be carried out in a calcination furnace connected to an extractor hood.
2. For the synthesis of the bulk gCN/PMA composite, the autoclave should be 3/5 full or even less to avoid high pressure.
3. Methanol (flammable, toxic, harmful) is used as a solvent and needs to be handled with caution and adequate protective gear.
4. After the solvothermal reaction, the autoclave must be completely cooled down before being opened (should be done in a fume hood, wearing gloves and nose cover) to prevent the uncontrolled release of toxic gases from the reactor.
5. The taste of the solvothermal mixture must be avoided.
6. Triethanol amine (used a a sacrificial agent) is a strong base and aquesous solutions should be handled wearing protective gear.
7. Hydrogen produced in the water splitting reaction is a flammable gas that can form explosive gas mixtures with oxygen.
8. When preparing the FTO film, deposition should be carried out in a fume hood to avoid the release of evaporated gases.

Doping method for the fabrication of P-doped gCN from PMA and gCN

In a typical procedure involving gCN and PMA, the synthesis of P-doped gCN was possible in 3 steps. The first step was the preparation of nanosheet gCN. Nanosheet graphitic carbon nitride (gCN) used in this study was obtained from cyanamide through a reported liquid exfoliation method of bulk-CN with modification.[1–3] Typically, covered crucibles containing appropriate amounts of cyanamide (CN) were heated at 500 °C for 4 hours in a muffle furnace under an Ar atmosphere at a 5 °C/min ramping rate. The resultant yellowish agglomerates were milled into powder in a ceramic mortar to get a bulk-CN powder. The bulk material was then transferred into a 250 ml conical flask containing a mixture of DW/IPA (3:1). The mixture was then placed in a sonicator bath for 30-45 min to proceed with the

liquid exfoliation process. After that, the milky solution was transferred into tubes and centrifuged at 8500 rpm and the aggregates were taken off from the whole milky solution. After drying at 65 °C overnight, the final powdered yellow sample was obtained as nanosheets of graphitic carbon nitride and labeled gCN.

The second step involved the synthesis of nanocomposite hybrid material made of Phosphomolybdic acid hydrate (Keggin POMs) and the as-prepared gCN above. This step was accomplished by a modified solvothermal method. Typically, 2 g of gCN was introduced into a 50 mL Teflon containing a 20 mL mixture of MeOH/DW (1:1) into which 1.5 g of PMA has been initially dissolved. After 20-30 min sonication, the sealed Teflon-lined stainless-steel autoclave was put in an oven, which was pre-set to 180 °C and heated for 13-17 hours. After cooling down to room temperature, the precipitate was collected from the autoclave and washed several times with a large amount of deionized water and three times with MeOH to remove any impurities and byproducts, especially the crystallized brown-white suspension coming from the reaction synthesis. This washing part is very important and the most sensitive part of the synthesis phase. Finally, a yellow-bright crystal product labeled as gCN/PMA1.5 was obtained and dried overnight at 60 °C in an oven. After drying, the gCN/PMA1.5 material was sieved to take out trace fine particles, and the final aggregate was carefully grounded in a ceramic mortar and used as the precursor of P-doped gCN. For comparison, different ratios of gCN/PMA have been synthesized using the same synthesis procedure with PMA content varying as 0.1; 0.2; 0.3; 0.4; 0.5; 1; 1.5; 2; 2.5 g.

The third step is the one that leads directly to the P-doped gCN material labeled as P-gCN/PMA_x. It simply involves post-annealing (post-calcination) of gCN/PMA_X. Typically, gCN/PMA_X is thermally annealed at 450 °C in a muffle furnace for 2 hours under an air atmosphere at a ramping rate of 5 °C/min. This step is also extremely sensitive and depends on the heating device (oven brand, status of the heating system) and the heating conditions one may require to set particular heating parameters. Failing to tune the heating conditions could lead to the complete sublimation of the sample. Performing thermal annealing in inert gas could help to improve the heating conditions. But in this work, this step has been performed in an air atmosphere. This annealing process results in the removal of the templating (molding) matrix and creates structural defects, and this results in the final material with changed optoelectronic properties. The final material is then characterized, analyzed, and tested for light absorption in the photocatalytic water-splitting process for the production of hydrogen.

Characterization

UV-Vis DRS measurements have been conducted to study the light absorption/diffraction ability of the prepared materials helping to determine the region and the maximum light-absorption intensity and to estimate by a simple calculation the optical bandgap (Eg) of the materials. X-ray photoelectron spectroscopy (XPS) combined with X-ray absorption spectroscopy (XAS) has been conducted for elemental composition measurements as well as for the electronic state of the atoms within materials. In addition, data collected from valence-XPS measurements have been used together with data from UV-Vis DRS to determine the band edge positions of the semiconductors that would, in turn, help to understand the band transition working mechanism of the photocatalyst. Photoluminescence spectroscopy (PL) measurements have been carried out to probe discrete energy levels in materials and extract valuable information helping to speculate on various wave-relaxation processes from where an idea about the charge separation and their recombination rate could be estimated. Combined with the time-resolved decay PL measurement, this analysis will help for the better demonstration of the improvement of the charge lifetime. For photocatalytic reactions, such a recombination phenomenon is extremely undesired, because the recombination of photoinduced electron-hole pairs decreases the quantum yield efficiency of the catalysts.[4,5] Additionally, qualitative and structural information was collected from Fourier Transform Infrared Spectroscopy (FTIR) measurements to examine the material and provide a prediction of its molecular structure (isomer). Additional structural information was collected from X-ray diffractometry (XRD) measurements to identify the crystalline phases; scanning electron microscopy (SEM) coupled with X-ray Energy dispersed microscopy (EDX) and transmission electron microscopy (TEM) for information about topography and morphology, microscopic and electronic composition, crystallographic aspect, atomic force microscopy (AFM) for mapping and providing a 3D topography of our samples. The surface area and pore size distribution of prepared materials have been determined through physisorption isotherm analysis using the Brunauer–Emmett–Teller (BET) equation.

Section 2: Additional discussions

Electronic microscopy analysis (SEM)

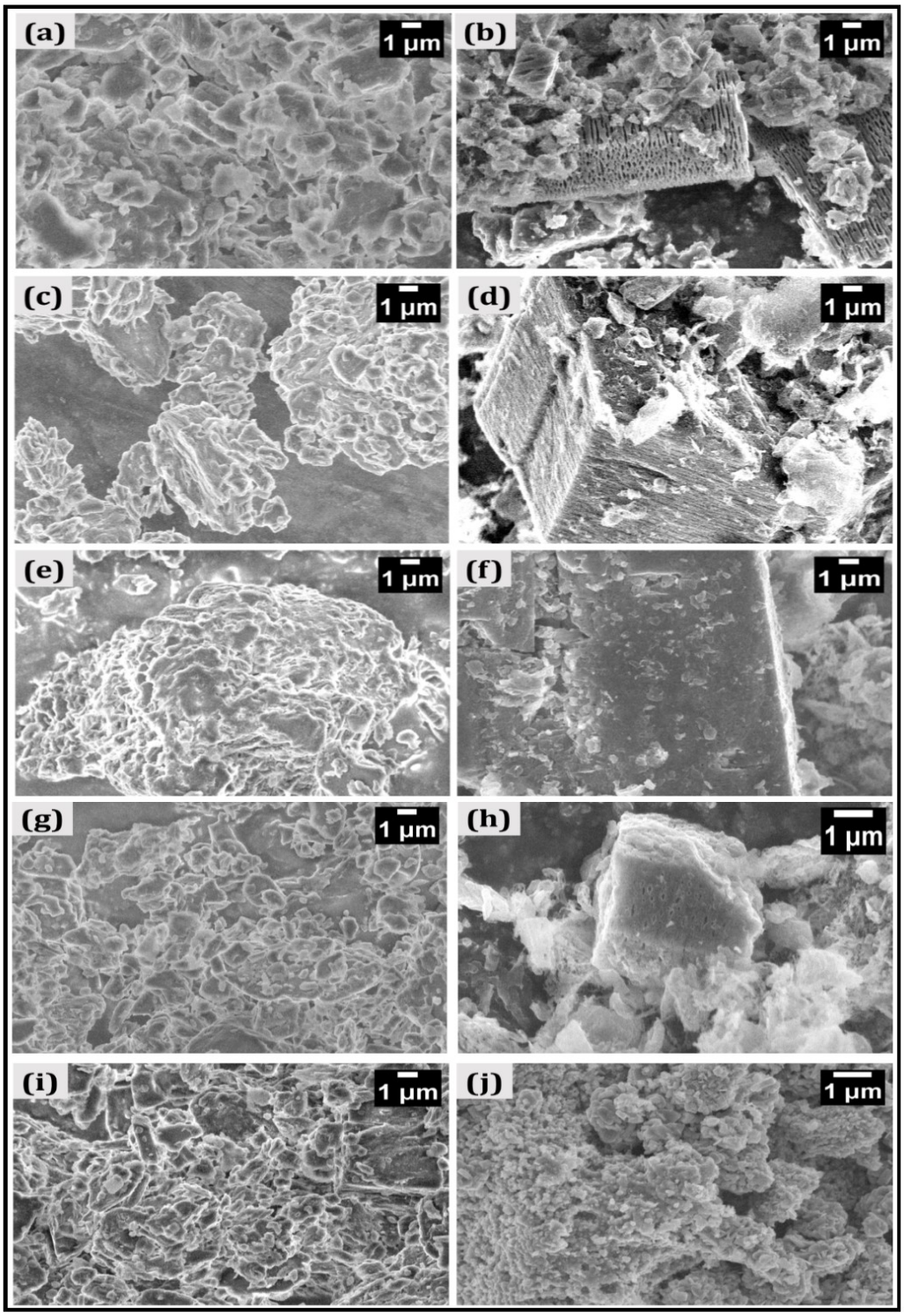

Figure SI 1: Comparison of SEM images of bulk composites (gCN/PMA$_x$): gCN/PMA$_{0.1}$ (a), (c) gCN/PMA$_{0.4}$, (e) gCN/PMA$_{0.5}$, (g) gCN/PMA$_1$, (i) gCN/PMA$_{2.5}$ with their corresponding P-gCN/PMA$_x$: (b) P-gCN/PMA$_{0.1}$, (d) P-gCN/PMA$_{0.4}$, P-(f) gCN/PMA$_{0.5}$, (h) P-gCN/PMA$_1$ and (j) P-gCN/PMA$_{2.5}$

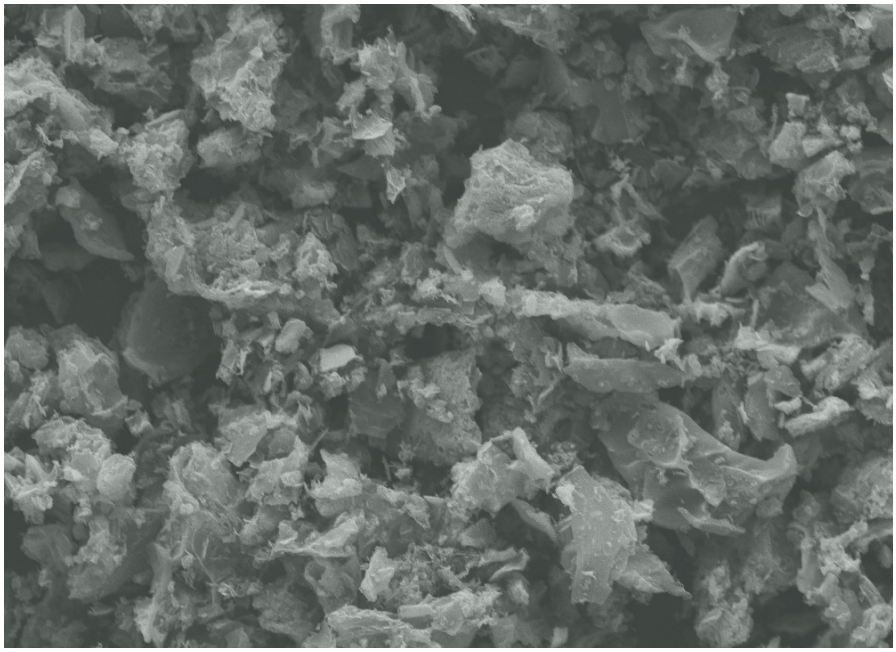

Figure SI 2: SEM of gCN

Regarding the above figures, it can be concluded that the gradual introduction of PMA in the bulk material has no significant effect on the physical aspect without proceeding further to the post-annealing step.

X-ray diffractometry (XRD) measurements

As reported in the literature, the FTIR spectrum of PMA (**Figure SI 5**) exhibits important characteristic bands around 1064, 964, 868, and 785 cm^{-1}, that are respectively ascribed to P-O, Mo-O-Mo, Mo=O_t, Mo-O_c-Mo, and Mo-O_e-Mo stretching vibrations (with t, c, and e referring to the terminal, corner and edge oxygens respectively).[6,7] Anyway, the subliminal information that should be kept in mind from this literature is that these IR peaks appearing in this range of PMA spectra indicate the presence of oxide molecules (oxygen bonded with P or Mo). Concerning this work, after the incorporation of PMA in gCN, the change of gCN structure is first reflected by the appearance of new characteristic bands in the gCN/PMA_X IR spectra from 500 to 1100 cm^{-1}, almost in the same range as for the PMA IR spectra as previously mentioned from the literature, which could be attributed to the formation of oxide molecules in the as-prepared bulk composite precursors. In addition, two characteristic bands are distinctively exhibited on gCN/PMA_X spectra around 3250 and 3400 cm^{-1} which are ascribed to O-H and N-H stretching vibration modes respectively owing to the partial acidification and water molecules absorbed during the solvothermal synthesis.

The more PMA is incorporated into gCN, the more the intensity of these wrinkled lines after thermal treatment (**Figure SI 7**). The broad peak in the region around 3000-3600 cm^{-1} indicates the presence of H-bonded species which is attributed to the stretching vibrational mode of N-H owing to partial condensation and O-H groups from the absorption of water molecules. This broadened band gradually becomes stronger and sharper with increasing PMA concentration along with solvothermal synthesis, resulting in the more ordered packing of doped tri-s-triazine motifs in the layers of nanosheets after the post-thermal treatment (**Figure 4d and Figure SI 7**). When the batch solution is saturated with PMA_x (PMA >1.5 g) along the solvothermal synthesis, the corresponding P-gCN/PMA_x FTIR spectrum is not similar to the gCN FTIR spectra (**Figures SI 6 and SI 7**) anymore. When the batch solution is saturated with PMA, the corresponding P-gCN/PMA_X FTIR spectrum comes closer to the PMA-450° FTIR spectrum, implying that gCN is destroyed (**Figure SI 6**).

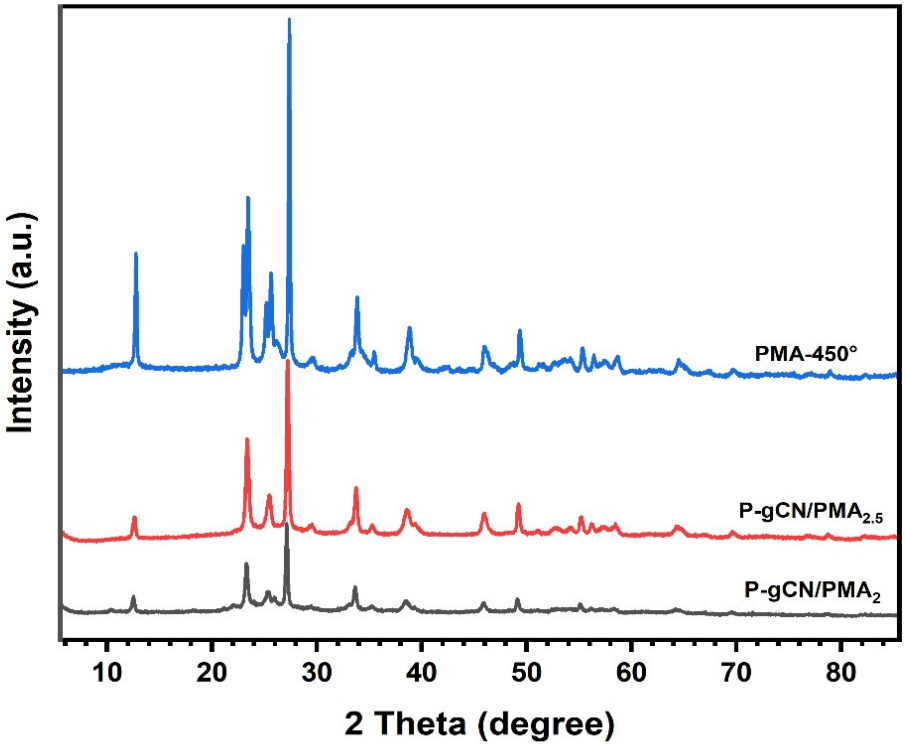

Figure SI 3: XRD patterns of P-gCN/PMA_2, (i) P-gCN/$PMA_{2.5}$ and PMA-450

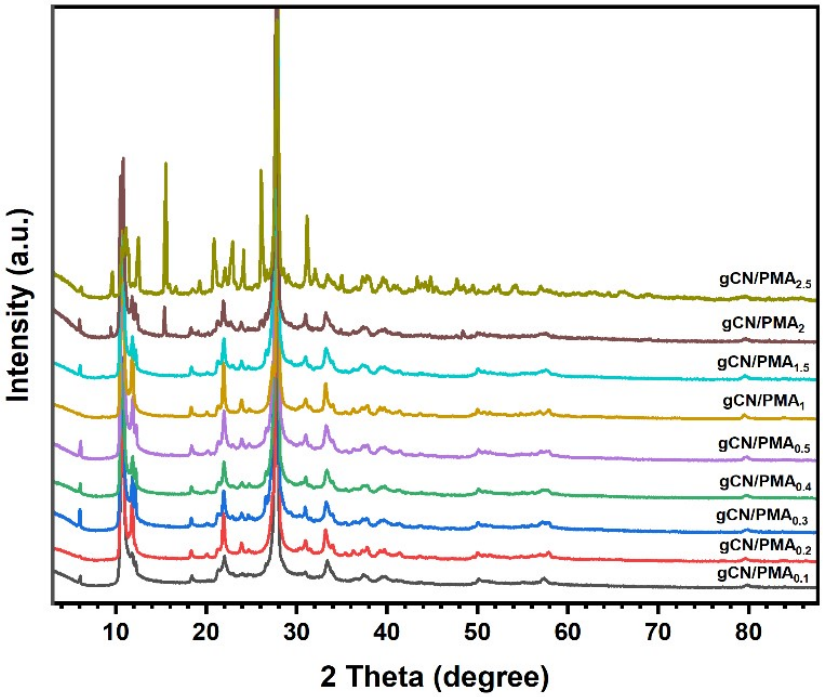

Figure SI 4: XRD patterns gCN/PMA$_{0.1}$, gCN/PMA$_{0.2}$, gCN/PMA$_{0.3}$, gCN/PMA$_{0.4}$, gCN/PMA$_{0.5}$, gCN/PMA$_{1}$, gCN/PMA$_{1.5}$ and gCN/PMA$_{2.5}$

FTIR measurements

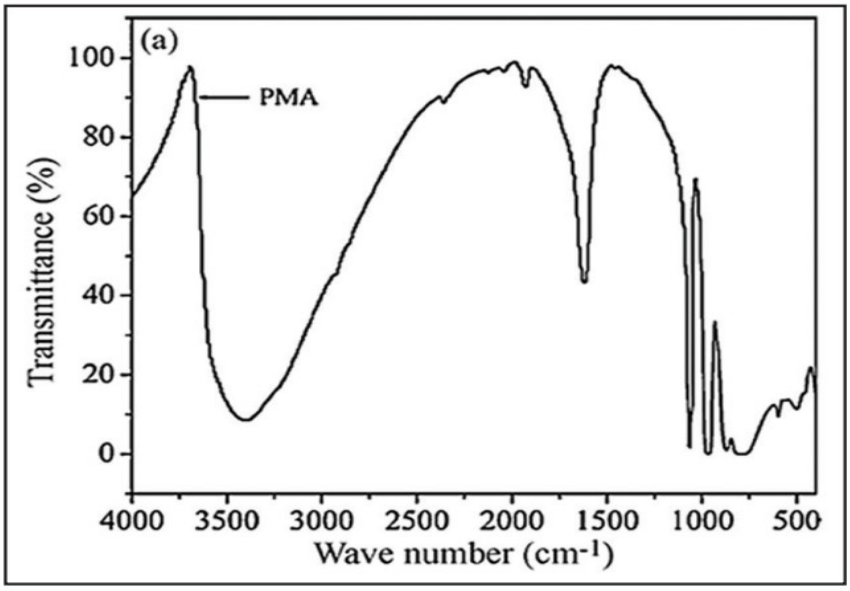

Figure SI 5: FT-IR spectrum of PMA[6,7]

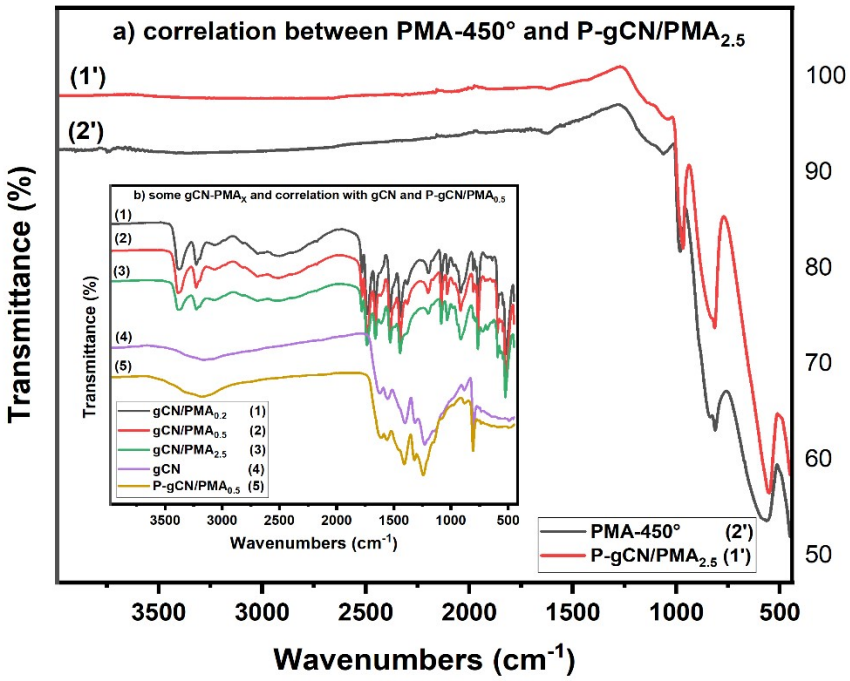

Figure SI 6: FT-IR spectra of gCN and P-gCN/$PMA_{0.5}$, gCN/$PMA_{0.2}$, gCN/$PMA_{0.5}$, gCN/$PMA_{2.5}$ in comparison with FT-IR spectra of PMA-450° and P-gCN/$PMA_{2.5}$

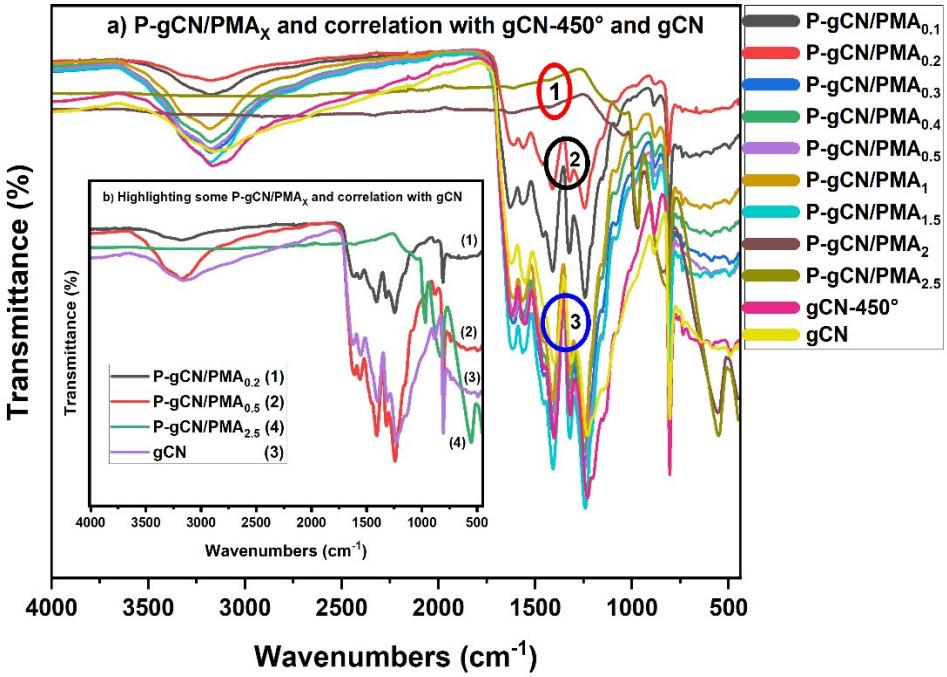

Figure SI 7: FT-IR spectra of gCN, gCN-450° C, and all P-gCN/PMA_x

However, to predict what could be the components of the heterojunction configuration, we performed FTIR of some samples and compared them with the IR spectrum of PMA calcinated at 450° C (**Figure SI 6** and **Figure SI 7**). PMA-450 and P-gCN/$PMA_{2.5}$ IR spectra exhibited peaks in the bending vibrations range similar to peaks exhibited in the same range by molybdenum oxide clusters as already

demonstrated in the literature[8,9]. This is proof that the gradual loading of the PMA until higher concentration during the solvothermal synthesis would lead to the formation of Molybdenum oxide by destroying the gCN backbone. As reported in Catalysis Letters Vol. 90, Nos. 1–2, September 2003 and Catalysis Letters 68 (2000) 223–227), the calcination of PMA at temperatures up to 450-500 °C clearly shows the formation of MoO_3 in FTIR spectra[8,9]. That helps to suspect the presence of MoO_3 which is well detectable at a higher fraction of PMA previously loaded and less or not detected at a lower fraction of PMA previously loaded. Then it can be assumed the most probable component of the heterojunction configuration is MoO_3. To know how this structure facilitates photocatalysis water splitting, it has to be speculated on how and where might it bind with the gCN backbone. Looking at the IR spectra of P-gCN/PMA_x (**Figure 4b**) in the range of 800-1200 cm^{-1} and 1450-1600 cm^{-1}, one should notice a slide difference as compared to gCN. The most interesting observation in this range is the appearance of several strong and wrinkled lines showing the vibrations of the metal-NC2 moiety resulting from the intercalation of metal ions. These wrinkled peaks might correspond to the bond vibrations of Mo-O resulting from molybdenum oxide molecules. Since these peaks are exhibited in between the stretching vibration modes of the aromatic CN from heterocyclic units, we can now assume that the MoO_3 from which the heterojunction configuration is provided is then bounded to the gCN backbone by establishing bonds with heterocyclic aromatic units. Regarding the IR patterns and the XRD patterns of each sample which do not discard so much from gCN, one can suggest the formation of coordination bonds. The presence of this component (MoO_3) within the gCN structure would better improve the photocatalytic water splitting by enhancing the electron transfer to the conduction band.

Gas adsorption studies

The average pore size determination was based on the Barrett–Joyner–Halenda (BJH) method and revealed the mesoporous structure of all samples. Sample size control and the effect of the variation of PMA on gCN were a bit problematic to understand. This situation could be explained by the non-uniformity and complex geometry provided by the cluster PMA, resulting in the non-chemical stability of the final material. The formation of big aggregates and the interparticle porosity after the post-thermal treatment also have a big effect on the average pore size distribution of the samples. This can also be seen in SEM results. Despite this situation, the introduction of PMA in gCN followed by post-thermal treatment helps at least to increase the S_{BET} of P-gCN/PMA_x compared to gCN.

Table SI 1: Characteristic values for P-modified samples

	$S_{BET}^{[a]}$	$P_S^{[b]}$	$P_V^{[c]}$	$E_g^{[d]}$
Sample Name	(m^2 g^{-1})	(nm)	(cm^3 g^{-1})	(eV)
P-gCN/PMA$_{0.1}$	33	11.3	0.18	3.02
P-gCN/PMA$_{0.2}$	30	13.4	0.2	3.01
P-gCN/PMA$_{0.3}$	23	11.6	0.128	3.01
P-gCN/PMA$_{0.4}$	84	12	0.510	2.97
P-gCN/PMA$_{0.5}$	20	20	0.358	2.98
P-gCN/PMA$_{1}$	48	15.3	0.358	2.46
P-gCN/PMA$_{1.5}$	59	11	0.317	2.70
P-gCN/PMA$_{2}$	1.81	30	0.052	-
P-gCN/PMA$_{2.5}$	1.03	11	0.012	-
gCN	10	17	0.06	2.87

[a]: Specific surface area ; [b]: Pore size radius; [c]: Pore volume; [d]: band gap energy.

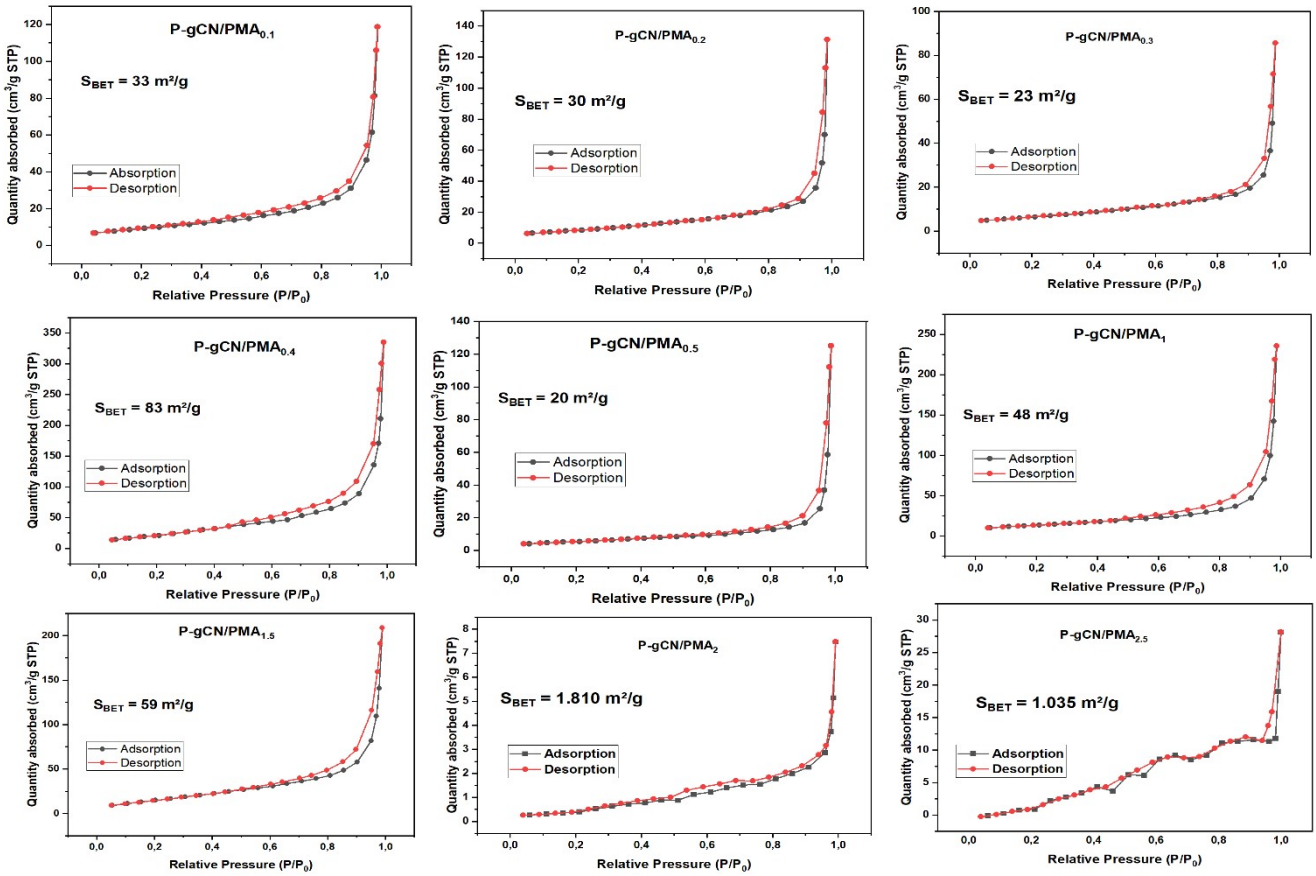

Figure SI 8: N_2 adsorption-desorption isotherms of as-prepared samples

Optical properties

At a higher amount of PMA, the absorption thresholds decrease a little, implying that bounded oxygen is involved in new transitions, revealing the occurrence of P heteroatoms. At a lower amount of PMA,

the amount of P atoms is not enough to exhibit a P-doping effect and that is the reason why the O-doping effect is more predominant. When increasing the amount of PMA, the P-doping effect is more significant, and the existence of cooperation between the P-doping phenomenon and the coordinated oxygen bounding effect from Mo-O-C_3N_4 leads to an in-situ hetero-junction construction, which provides higher electronic properties to the corresponding photocatalyst composite.[10] When the bulk solution was extremely saturated by PMA (x > 1.5 g), no specific absorption was observed for P-gCN/PMA_x (the absorption signal was frizzy) despite their corresponding bulk gCN/PMA_x composite exhibited absorption signal (**Figure SI 10**).

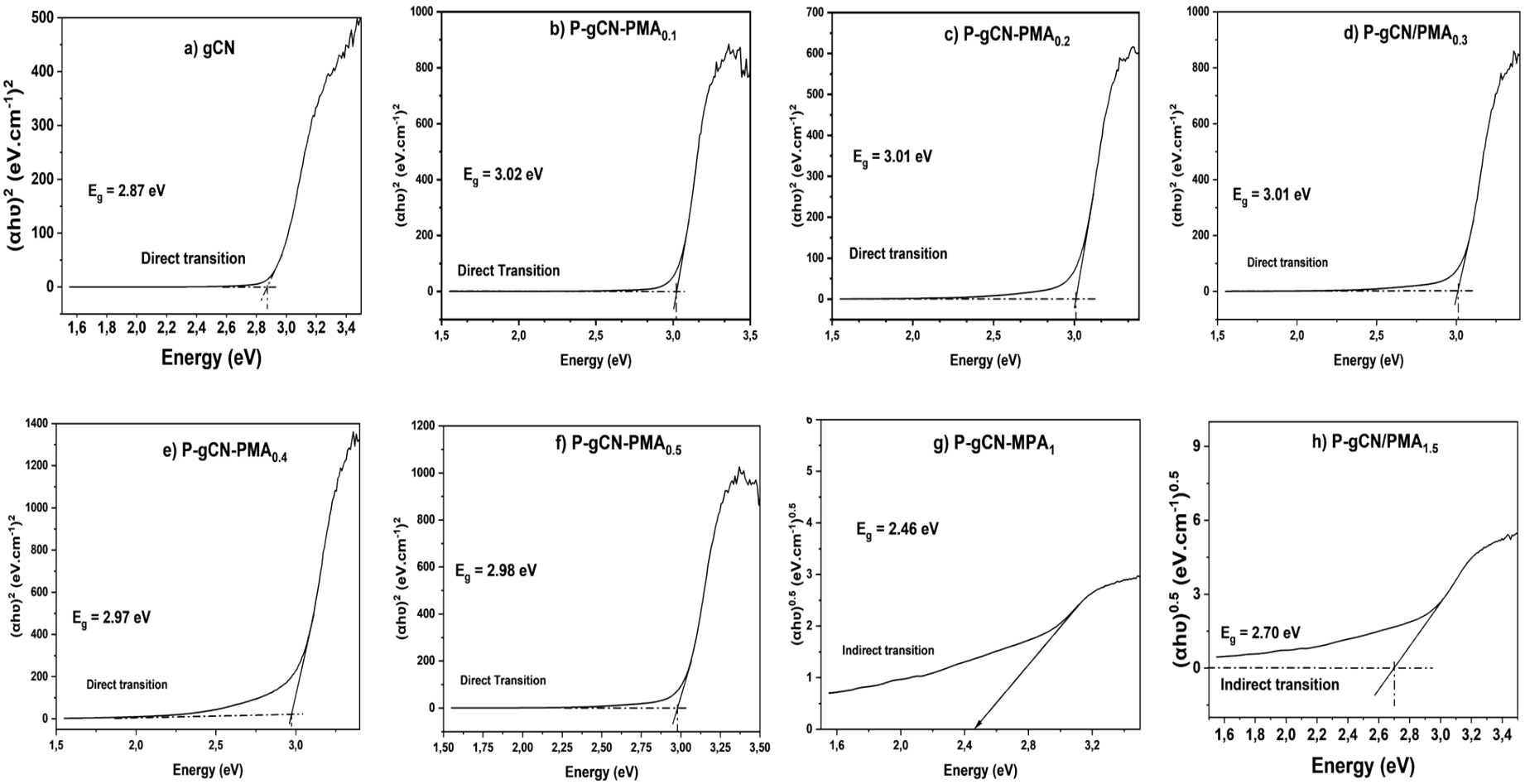

Figure SI 9: Band energy estimation of gCN (a) and P-gCN/PMA$_x$ (b-h).

The band gap energies were evaluated by the potting $[F(R).(h\upsilon)]^{\frac{1}{n}} = A(h\upsilon - E_g)$ (eq. 1) against $h\upsilon$ employing the well-known Tauc's procedure[11,12] by considering direct and indirect transitions. The band gap energies of the different samples were determined from the intercept of the tangents with the x-axis from each plot. As shown in **Figure SI 10**, the raw gCN/PMA$_x$ used as a composite precursor exhibited a very short absorption tail in the range above 450 nm and exhibited no HER under light irradiation. The post-thermal treatment helps to get back the interesting P-gCN/PMA$_x$ material with many defects and with large and longer absorption tails together with a tuned and improved crystalline structure. As a result, more charge carriers can transfer more easily across the nanosheets with limited recombination. The above-mentioned observations are consistent with previous reports that the conjugated polymer doped with heterogeneous elements tends to decrease the band gap and the post-thermal treatment is the best experimental factor that might enable the doping polymerization effect.[10,13–15]

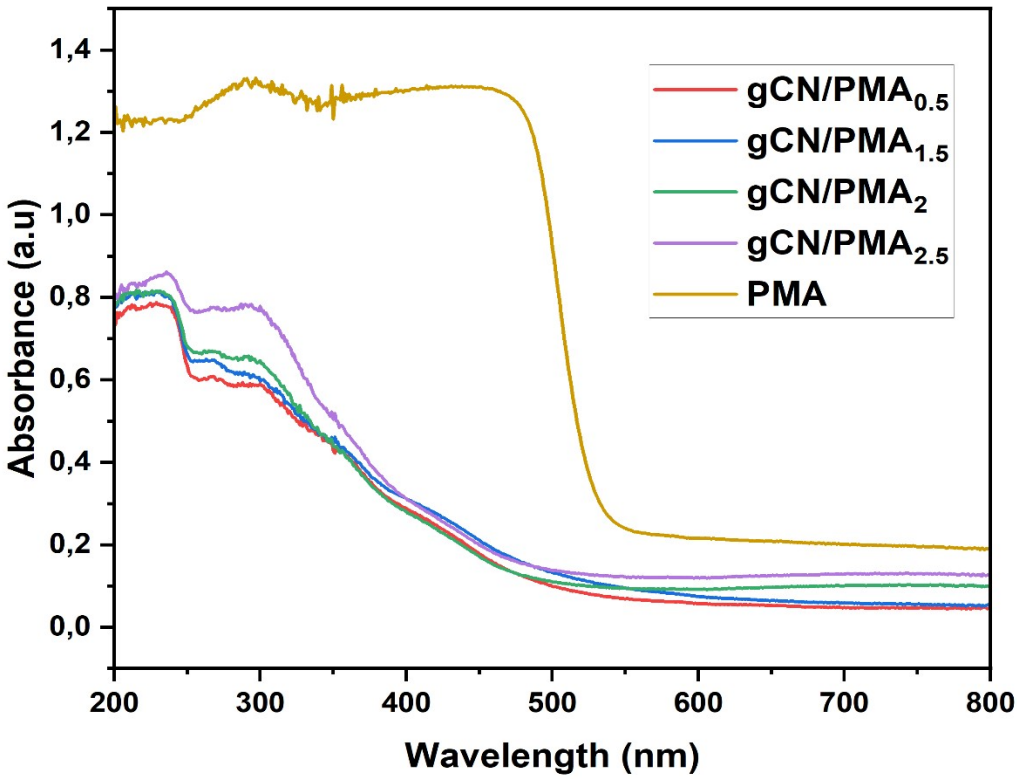

Figure SI 10: UV-vis diffuse absorption spectra

From **Figure SI 9**, one can notice that the incorporation of elements through PMA has a direct effect on the absorption energy of the final modified gCN. The band gap energy rises from 2.87 eV for gCN to 3.01 eV for P-gCN/PMA$_{0.1}$ keeping the transitions in the direct mode. From previously reported works[16–18] and corresponding analogies, the raising of band gap energy might be explained by the

fact that the POM used is a polyatomic complex dominated by anionic ligands that oxidize the core pattern (gCN) giving lower and weak bond to the band transition structure of the final network due to the VB typically dominated by O_{2P} states which are about 3 eV lower than the H_2/H_2O level.

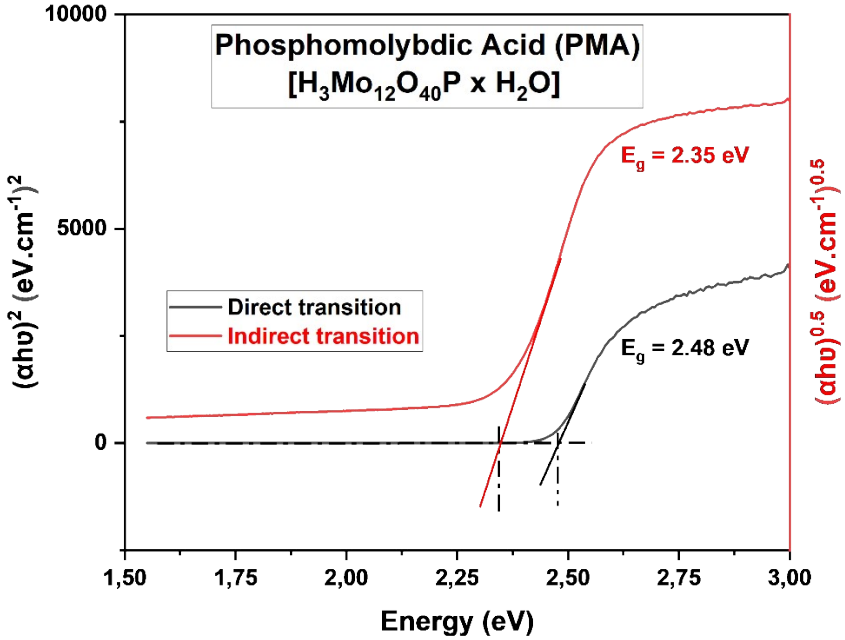

Figure SI 11: Direct and indirect band energy estimation of PMA.

Electronic properties investigations

Figures SI 12 and SI 13 display the XPS survey and high-resolution spectra of selected gCN/PMA_x composite precursors in comparison with gCN. XPS survey spectra revealed the existence of O, C, and N elements in gCN. Although peak intensities change from one sample to another, this survey spectrum indicates that all bulk gCN/PMA_x precursors are composed of C, N, O, Mo, and P elements confirming that doping elements are effectively released from the supramolecular cluster (POM) for the modification of gCN framework. However, Mo and P peaks are not easily observable on the survey spectra of every bulk precursor implying that, at this synthesis stage, all carbon residues from the gCN framework were not able to react completely with elements provided by PMA and this resulted in a weak bonding area surrounding these elements inside the bulk gCN/PMA_x composite precursors. By performing the high-resolution spectra (**Figure SI 12**) of the above-mentioned elements, it was able to demonstrate the evidence of Mo and P and how high C 1s have been affected by the reaction when increasing the concentration of PMA in the bulk solution. gCN/$PMA_{1.5}$ exhibits the highest Mo and P intensities without stronger alteration of the gCN framework. This situation could be explained by the fact that, at this concentration, the *p* and *d* orbitals are much more available and possess more energy to dominate the *s* orbitals followed by a strong hybridization of gCN.

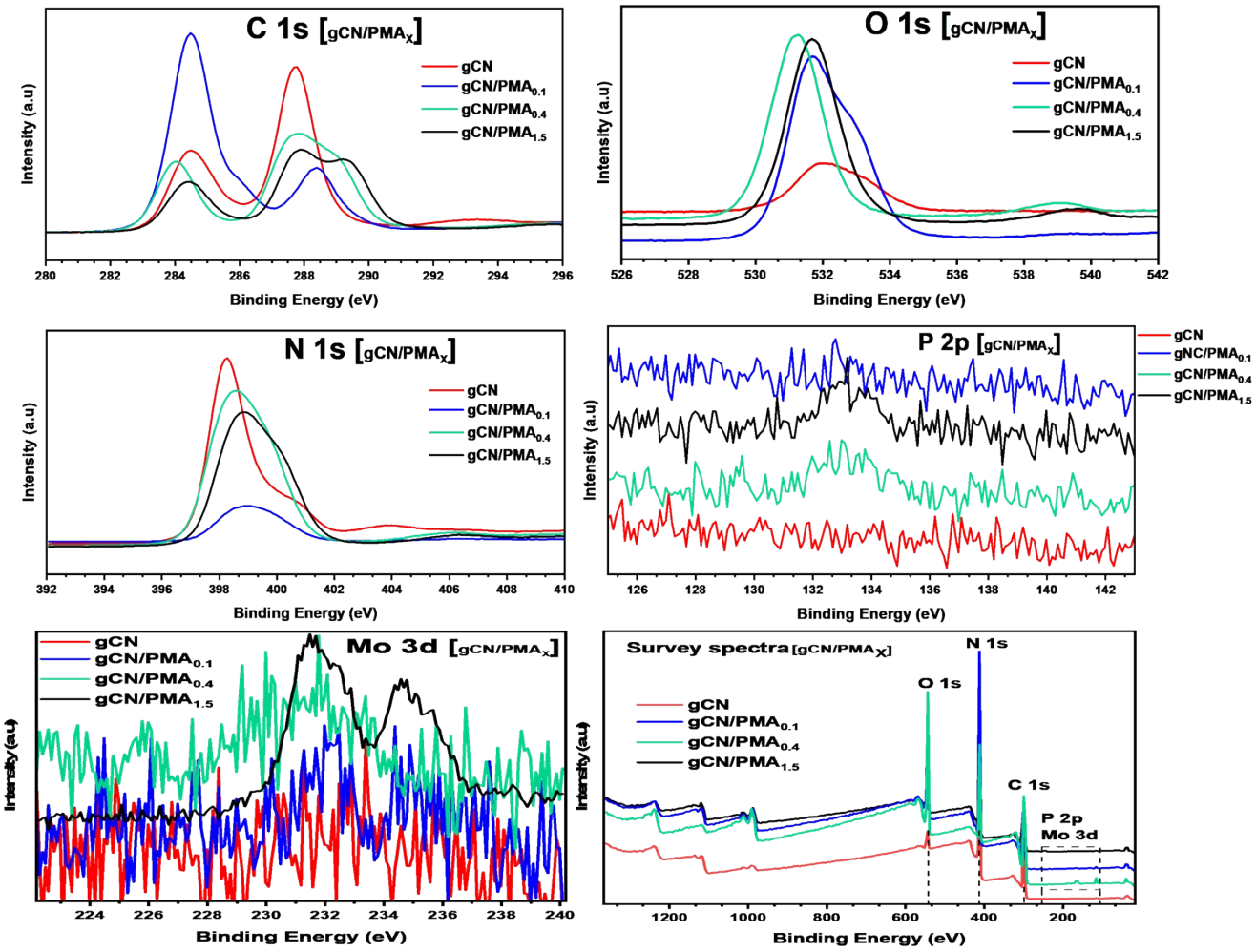

Figure SI 12: XPS survey spectra, high-resolution XPS spectra of C 1s, O 1s, N 1s, P 2p, and Mo 3d for the bulk gCN/PMA$_x$ composite precursors

This may probably result in a strong C and N attack followed by the formation of intermediate mid-gap states which are generated as a result of P doping by the hybridization of C 1s and/or N 1s. However, unreacted intermediates with their undesired orbitals may exhibit minor transition states in the whole electronic system of samples that poison the desired electronic states and further inhibit excited species which are needed in the VB and CB for redox reactions. This electronic behavior makes gCN/PMA$_x$ non-photochemically active for the photocatalytic HER. In practice, it was observed observed this inactivity by the fact that all gCN/PMA$_x$ exhibited no HER under UV and Vis light irradiation despite their suitable band gap energy. To recover its photocatalytic activity for efficient HER, all bulk gCN/PMA$_x$ composite need to be purified to take out unreacted intermediates together with all impurities, to make available all desired transitions for photocatalytic HER enhancement. This treatment has been performed by thermal annealing of gCN/PMAx composite precursors in the air-atmosphere at a specific temperature and the final P-gCN/PMA$_x$ catalyst has been obtained with higher optoelectronic properties and efficient photocatalytic activity for HER.

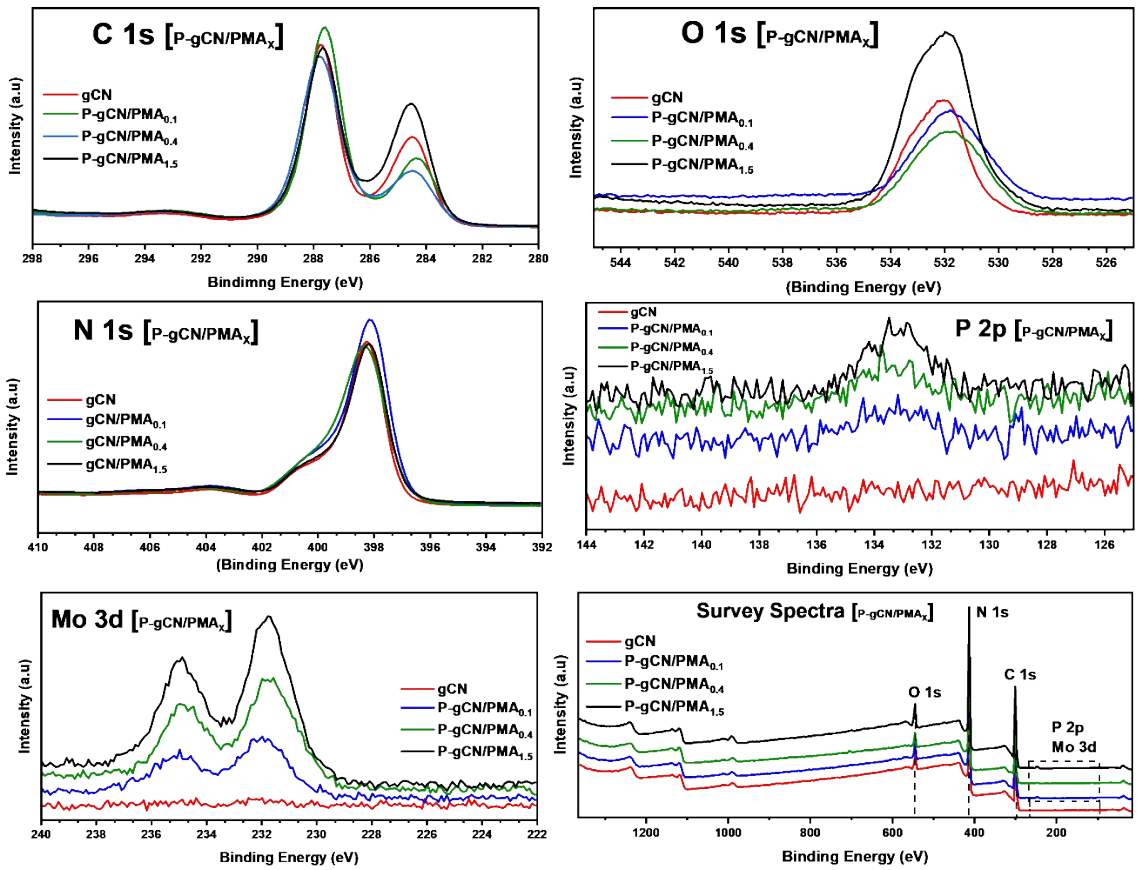

Figure SI 13: XPS survey spectra, high-resolution XPS spectra of C 1s, O 1s, N 1s, P 2p, and Mo 3d for the P-gCN/PMA$_x$ catalyst materials

Figure 6 and Figure SI 13 display the XPS survey and high-resolution spectra of some P-gCN/PMA$_x$ in comparison with gCN. The P-gCN/PMA$_x$ survey spectra re-confirm the evidence of C, N, O, P, and Mo atoms in the final material obtained after post-annealing of the corresponding bulk gCN/PMA$_x$ precursor. Moreover, the threshold intensities of Mo and P atoms are higher and displayed on their high-resolution XPS spectra (**Figure 6**) and the smoothing of these XPS curves confirms the removal of all impurities and unwanted transitions by the thermal treatment procedure. From the electronic point of view (**Figure 6, and Figure 5d**), sample P-gCN/PMA$_{1.5}$ is suspected to be the best one from which the P-doping effect together with the hetero-junction construction might be beneficial for photocatalytic application. For a better and easy interpretation, **Figure SI 13** displays high-resolution XPS of P-gCN/PMA$_{1.5}$ highlighting the comparison with its exhibited orbitals and its corresponding composite precursors and gCN. By observing the spectral pattern exhibited by C 1s, one understand that the direct introduction of POMs into gCN pattern completely changes the structure of gCN and as a result, its photoactivity is completely lost even if new elements are being provided in the bulk composite precursor. This non-activity could be explained by the presence of several impurities (basically heavy oxide molecules) which hide the desired optical transitions by the misleading transitions with the help of some electrons located in dominant orbitals. C 1s of P-gCN/PMA$_{1.5}$ exhibits a similar spectral pattern to C 1s of gCN but with different intensity implying

that, after the incorporation of elements from POMs, the thermal annealing helps to recover the gCN backbone with new and beneficial optical properties. This could be explained by the fact that there is suitable cooperation between existing orbitals in which d orbitals are also involved and further, some atoms from gCN have been substituted by an equivalent amount of P atoms confirming the possibility of constructing a hetero-junction bridge. A similar observation could be done with orbitals from N and O atoms (**Figure SI 13).**

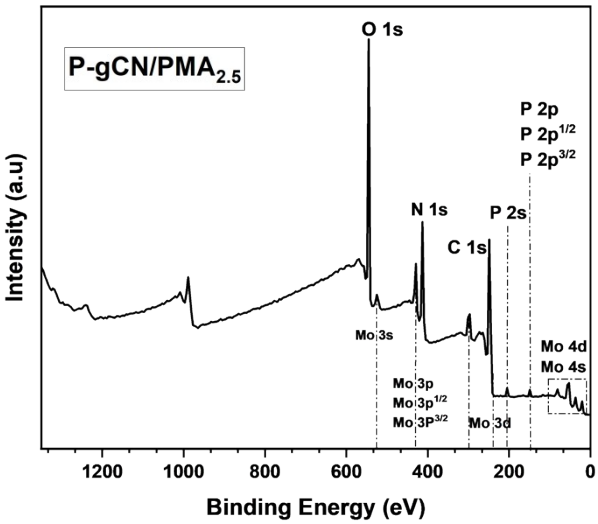

Figure SI 14: XPS survey spectra of P-gCN/PMA$_{2.5}$ catalyst proving the evidence of Mo and P

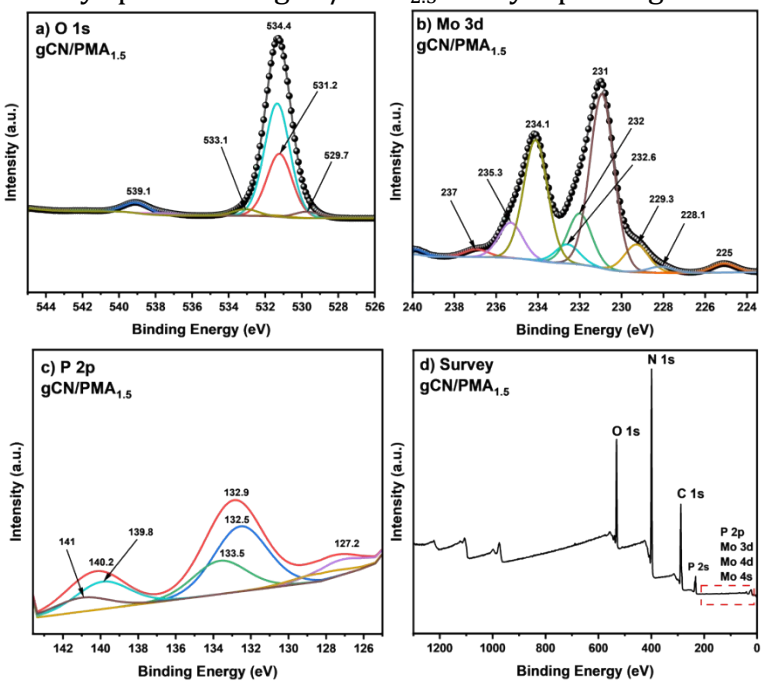

Figure SI 15: Survey and High-resolution deconvoluted XPS spectra of O 1s, P 2p, and Mo 3d for gCN/PMA$_{1.5}$

Electronic Band Structure

In **Figure 5d**, by fitting/extrapolating the linear parts of the band tail edges of the VB XPS spectra, the VB-XPS values have been estimated. Sample P-gCN/$PMA_{1.5}$ shows a band tail with its end at 1.40 eV corresponding to its VB-XPS energy. This value is much higher than the VB-XPS of gCN (1.29 eV) and other P-gCN/PMA_x samples from the graph. This higher VB-XPS suggests a presence of dangling bonds and stronger oxidation of the photogenerated holes in P-gCN/$PMA_{1.5}$ caused by PMA (POM) that had released many oxidation species during the solvothermal phase of the synthesis.[19] The valence band potentials E_{VB} were calculated by using equation (2) and by taking the vacuum level as energy reference, where Φ is the electron work function of the analyzer instrument set at 4.35 eV. Data of the calculated E_{VB} for vacuum energy level are summarized in **Table SI 2**.

$$E_{VB\text{-}potential} = -(\Phi + VB_{XPS}) \quad (2)$$

Combining the optical band gap of every sample from the UV-Vis DRS results, the values of conduction band potential (CB) are deduced according to the following equation, $E_g = | E_{VB} - E_{CB} |$ and also listed in **Table SI 2**. Furthermore, by using the calculated VB-potential and CB-potential, the valence band maxima position (VBM) and conduction band minima position (CBM) of every sample were predicted to be located on the potential band diagram energy (**Figure 7**) by taking the reduction valence potential of hydrogen as E_{VB} (H^+/H_2) = -3.85 eV (at pH= 10.7)[20] and calculated from derived Nernst equation ($E_{red} = -0.05916\ pH$)[21] of hydrogen reduction potential by considering the standard hydrogen electrode (SHE) as 4.44 eV below the vacuum energy level.

The decrease of the CB suggests an electronic dominant effect from p-orbitals over s-orbitals.[14,15] This observation means that the CB in electronic band structures of P-gCN/PMA_x materials could be tuned by manipulating the P-doping element contained in PMA. The contributions of substituted carbon might have a direct consequence on the decreased balances of ***π***-conjugated electrons of triazine rings and thus reduced the band gaps of the large doped sample. The results suggest that the synthesis method employed in this work helps to simultaneously provide the P-doping effect, heterojunction construction, and defect structures. It is mentioned that the existence of point defect structures is evidence of mid-gap states, which are also referred to in other literature as defect states, deep energy level defects, deep traps, deep defects, and mid-gap defects, related all together to atoms near the vacancy sites.

Table SI 2: XPS valence band values with VBM and CBM

Samples	E_g (eV)	$E_{VB\text{-}XPS}$ (eV)	E_{VBM} (eV)	E_{CBM} (eV)
gCN	2.87	1.29	-5.64	-2.77
P-gCN/PMA$_{0.1}$	3.02	1.32	-5.67	-2.65
P-gCN/PMA$_{0.4}$	2.97	1.34	-5.69	-2.72
P-gCN/PMA$_{0.5}$	2.98	1.36	-5.71	-2.73
P-gCN/PMA$_{1.5}$	2.70	1.40	-5.75	-3.05

Table SI 3 summarizes the elemental composition of selected P-gCN/PMA$_x$ samples. The elemental balance was performed using a combination of ICP-OES, CEA, EDX, and XPS techniques. Based on this table, it is important to note that the weight percentage of oxygen increases strongly with the loaded fraction of PMA at the solvothermal phase. This confirms the presence of metal oxides or the formation of phosphates in the final complex. Alluding to the doping phenomenon, the small decrease in carbon and the small increase in phosphorus (XPS, CEA) allows us to highlight a substitution of carbon atoms by phosphorus atoms. This can be observed for every P-gCN/PMA catalyst with PMA fractions lower than 1.5 g in the solvothermal phase. For loaded PMA fractions higher than 1.5 g, a brutal and wild poisoning of the gCN building block is observed, destroying completely the support material.

Table SI 3: Elemental composition of samples analyzed from ICP-OES, EDX, XPS, and CEA technique

Samples	Elements (% wt)															
	ICP-OES & CEA						EDX					XPS				
	C	N	O	H	Mo	P	C	N	O	Mo	P	C	N	O	Mo	P
P-gCN/PMA$_{2.5}$	16.45	29.15	-	1.19	12.8	3.8	12	3.3	73.6	9.62	1.4	15.1	24.9	46.4	10.7	2.9
P-gCN/PMA$_{1.5}$	29.45	52.41	-	2.02	0.85	0,61	31.2	58.1	4.7	0.04	0.01	40.4	56.4	2.9	0.18	0.12
P-gCN/PMA$_{0.5}$	32.19	55.69	-	1.94	0,22	0,12	33.2	64.7	3.9	0.01	-	43.1	54.1	2.71	0.07	0.02
P-gCN/PMA$_{0.4}$	32.63	58.49	-	1.89	0,10	0,06	30	67.1	2.8	-	-	42.6	53.9	3.46	0.03	0.01
P-gCN/PMA$_{0.1}$	32.54	58.92	-	2.27	0.04	-	30.5	66.5	2.9	-	-	42.9	53	3.9	0,02	-
gCN	33.43	60.05	0.0	2	-	-	30.9	66.5	2.5	-	-	45.80	50.71	3.49	-	-

Photoluminescence emission measurements

As PL emission spectra of photocatalysts are mainly used as an indicator of the recombination or separation efficiency of photogenerated charge carriers, it is widely demonstrated that the rate of electrons-hole pairs separation and their recombination rates are directly proportional to the intensity of the luminescence peak.[4] In other words, faster recombination of electron-hole results in a more intense PL spectrum. Photoluminescence (PL) spectroscopy was carried out using a Varian Cary Eclipse fluorometer with different excitation wavelengths of 320nm, 370 nm, and 400 nm. The best PL spectra were obtained with an excitation wavelength of 400 nm as shown in **Figure 5e**.

A closer examination of the PL spectra shows that there is a small shift of the PL P-gCN/$PMA_{1.5}$ peak to the left (lower wavelength). This can be ascribed to the incorporation of Mo ions into the gCN lattice structure. In P-gCN/$PMA_{1.5}$ 3D nanosheets, we may have the formation Mo-gCN coordinated bond, hence Molybdenum may act as the photogenerated electron target to reduce the recombination of photogenerated electron–hole pairs.[22]

Section 3: Photocatalytic experiments

Application to photocatalytic H_2 production

For better optimization of hydrogen production, photocatalytic experiments have been performed in several stages. The first stage of the photocatalysis experiment consisted of screening samples; this was performed by measurering the hydrogen evolved by each P-gCN/PMA_x sample to see which of those samples exhibited the highest performance. This has been done with the help of a one-slide-double-walled side-planar-irradiation quartz reactor of a total volume of Vo = 35 mL connected to a thermostat that was set to 25° C for the water circulating cooling system. In the practice, 10 mg of every P-gCN/PMA_x sample was transferred in the reactor vessel and dispersed by 1 min sonication in a mixture of water and triethanolamine (used as sacrificial agent) in a volume ratio of 16:2 mL (H_2O/TEOA). Then 10 μL of H_2PtCl_6 aqueous solution (8 wt%) are added to the reactor as the source of Pt co-catalyst. After sealing the reactor with rubber stoppers, the dispersion was flushed/degassed by Argon for 15-20 minutes to remove air and to ensure that the reaction system remained under anaerobic conditions before the irradiation. The irradiation was then carried out with a 300 W Xe arc lamp through a 395 nm cut-off filter aiming to stay near visible light conditions. The beam light exit of the lamp was positioned 10 cm away from the reactor to trigger the photocatalytic reaction under constant stirring of the photocatlyst suspension. The focused intensity on the flask was *ca.* 180 $mW.cm^{-2}$. The photocatalytic experimental setup is well described in **Figure SI 16**. The reactor was kept under irradiation for 3 hours and then, 4 mL of gas sample was taken from the headspace through the rubber septum with the help of a gas-tight syringe, and hydrogen was analyzed and quantified by GC (Agilent Technologies 7890A) equipped with a thermal conductivity detector. Ultra-pure water was used in all photocatalytic experiments, every sample was tested 3 times for HER under light irradiation to ensure the reliability of data and the repeatability of the experiments. All sampled gas from the reactor was analyzed and quantified by GC in 2 runs to ensure the accuracy of data and to minimize eventual errors. Then, the hydrogen production rate (equation 3) and the volume amount of hydrogen produced (equation 4) after irradiation were estimated by simple calculation from the volume percentage obtained from GC according to the following equation well developed in literature.[23]

$$\dot{n}_{H_2}(Reaction) = \frac{(V_0 - V_L)\, P_2\, x\, H_2\, (GC)}{P_1\, (m_{cat}\, x\, t_R)\, x\, V_m} \qquad (3)$$

$$n_{H_2}(Reaction) = \frac{(V_0 - V_L)\, P_2\, x\, H_2\, (GC)}{P_1\, m_{cat}\, x\, V_m} \qquad (4)$$

In these equations, V_0 stands for the total volume required to fill up the reactor when sealed (35 mL), P_2 is the pressure in the reactor, P_1 is the atmospheric pressure, V_L stands for the volume of the liquid phase undergoing the photocatalytic experiment (18 mL), H_2 (GC) is the concentration of H_2 in the gas phase quantified by GC and given in volume percentage from the total gas detected by the analyzer, m_{cat} is the mass of the catalyst (10 mg) introduced in the reactor, t_R stands for reaction time under irradiation for photocatalytic reaction and V_m is the molar volume of hydrogen at a given temperature (24 $L.mol^{-1}$). The amount of hydrogen produced according to each sample and calculated from GC recorded data are summarized in **Figure 8a**. After photocatalytic experiments, all the used P-gCN/PMA_x were recovered by vacuum filtration, washed with water and ethanol to remove all byproducts, and the collected samples were dried at 65 °C overnight in a vacuum atmosphere for further characterization and/or for reuse.

The catalyst loses its photocatalytic HER activity when the raw solution is saturated with PMA during the solvothermal phase. This can be observed in **Figure 8a**, samples P-gCN/PMA_2 and P-gCN/$PMA_{2.5}$ exhibited no HER, as the GC analyzer detected no hydrogen. This could be explained by several factors: the destruction of the gCN framework due to its strong oxidation caused by the overloading of oxo radicals from PMA, which results in the elimination of reduction sites where the H^+ reduction reaction was supposed to take place. This improves the oxidation sites where the water oxidation would take place for the enhancement of the oxygen evolution reaction (OER). At higher concentrations of PMA, the P-doping effect is dominated by an advanced heterojunction phenomenon and the final catalyst looks much more suitable for OER.

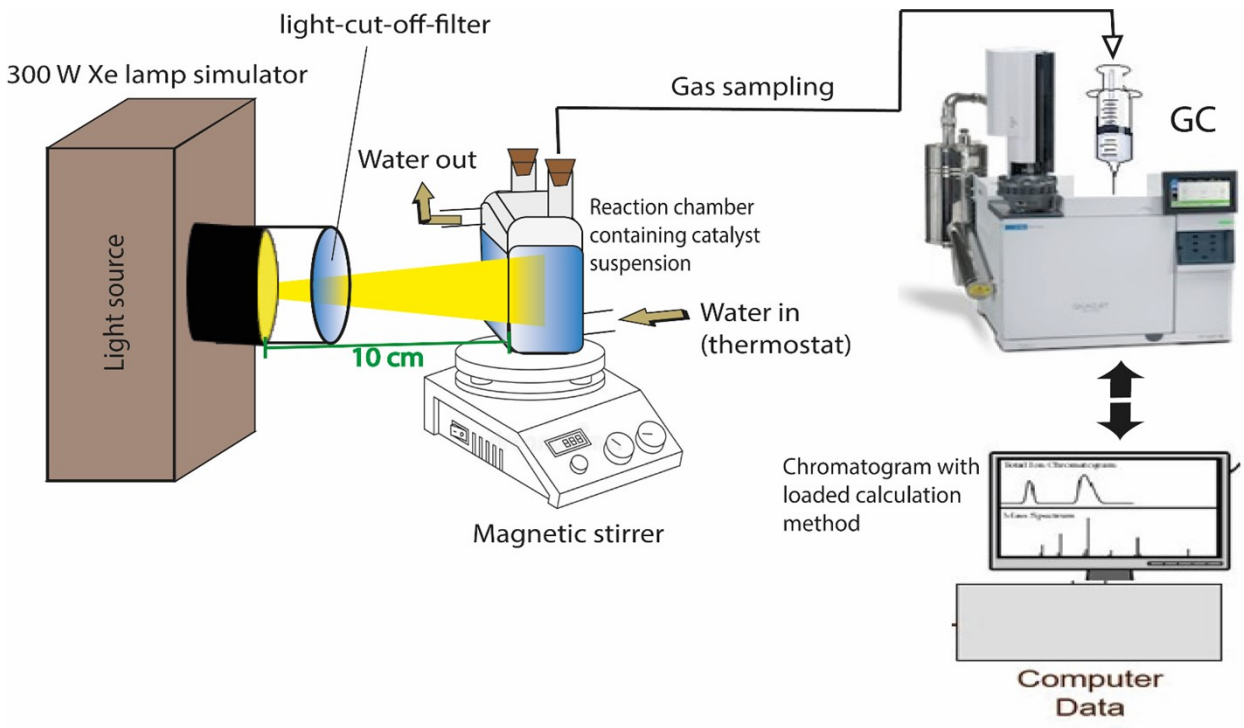

Figure SI 16: Laboratory set up for the photocatalytic HER testing

Mass of catalyst and temperature effect on H_2 evolution

Another photocatalysis experiment consisted of the study of the effect of catalyst mass variation on the hydrogen production yield. To perform this task, the most efficient sample among P-gCN/PMA_x samples, which means the one through which the most successful hydrogen production has been exhibited, was selected. From the above-mentioned stage 1, the P-gCN/$PMA_{1.5}$ sample was proven to be the most successful one that matches well with the needs. Thus, to perform investigations on the mass effect, all photocatalytic experimental conditions from stage 1 have been kept unchanged but, only the mass of P-gCN/$PMA_{1.5}$ catalyst was varied from 0.01, 0.02, 0.03, 0.04, and 0.05 g for every photocatalytic reaction and the results of H_2 evolved are summarized in **Figure SI 17a**.

From **Figure SI 17a**, it is observed that the change of mass catalyst has no significant effect on the photocatalytic HER performances both for gCN and P-gCN/$PMA_{1.5}$. This confirms that the HER performances do not depend too much on the contact surface of light with the material catalyst but that it mainly depends on the electronic structure of the catalyst and the availability of reaction sites. This implies that the successful tuning of the electronic structure as mentioned above might be enough for the efficient improvement of HER performances. However, the optimal performance is obtained for 0.05 g of P-gCN/$PMA_{1.5}$ (729 μmol.g^{-1}.h^{-1}) but, the gap was not too high as compared to HER performances for 0.03 g of P-gCN/$PMA_{1.5}$ (684 μmol.g^{-1}.h^{-1}). Considering the size of the reactor (35 mL), working with 0.01 g of P-gCN/$PMA_{1.5}$ might be much more favorable for the

photocatalytic reaction because it would be easier for the incident light to penetrate the interior of the catalyst to get absorbed by photons and generate photo-excited species that would be easily transferred to the material surface for redox reactions.

Another stage of the photocatalysis experiment consisted of the study effect of the reactor temperature on the hydrogen production yield. Thus, to perform this task, all photocatalytic experimental conditions from stage 1 were kept unchanged and P-gCN/PMA$_{1.5}$ was used as a catalyst but, only the temperature of the reactor was varied from 20, 25, 30, 35, 40, 45, and 50° C with the help of thermostat for every photocatalytic reaction and results of H_2 evolved are summarized in **Figure SI 17b**. The increase in temperature has a strong significant effect on both catalysts for HER performances. This effect is strongly pronounced on P-gCN/PMA$_{1.5}$. At 20-50° C reaction temperature, the photoactivity of P-gCN/PMA$_{1.5}$ rapidly increased for HER with the increase in reaction temperature, this advantageous situation could be explained by the fact that after the synthesis, we got a material with a new electronic structure that possesses better electronic properties due to the introduction of new elements together with new bonds. Then, the increase in reaction temperature would directly influence the quantum effect thus, the electron-hole separation would be better enhanced at higher temperatures and the recombination process would be minimized.[24] The optimal temperature of 50° C is regarded as the ideal temperature for optimal HER performances and might be appropriate for large-scale applications. The evolved hydrogen from P-gCN/PMA$_{1.5}$ at 50° C with a reaction rate of 1157 μmol.g^{-1}.h^{-1} is almost 3.5 times higher than the one evolved by gCN at the same temperature (349.2 μmol.g^{-1}.h^{-1}).

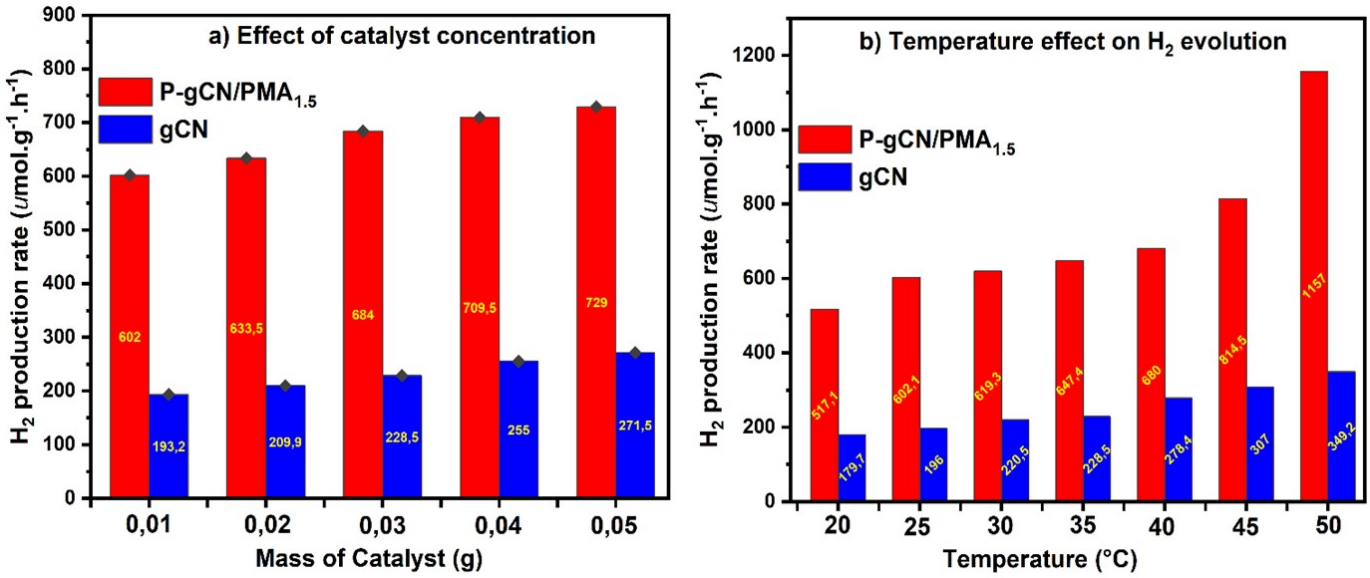

Figure SI 17: Effect of P-gCN/PMA1.5 concentration (a) and effect of temperature (b) on the H_2 evolution performances

The next stage involved reaction rate investigation of photocatalytic hydrogen evolution. This was done by monitoring the hydrogen evolved after specific time intervals. In practice, 10 mg of P-gCN/$PMA_{1.5}$ sample were used and reaction conditions of stage 1 were kept unchanged except for the irradiation time. After triggering the photocatalytic reaction by the light source, 1 mL gas was intermittently sampled (in every hour of time irradiation) for a total exposure duration of 6 hours, and results are shown in **Figure 8b**. One can suggest that by tuning the amount of gCN in the bulk solution at the solvothermal phase it could be possible to better improve the cooperation between the doping effect and heterojunction phenomenon during the post-thermal phase and to further improve the electronic structure of the final catalyst together with its photocatalytic activity. Successful photo-deposition of Pt co-catalyst is also known as one of the key factors of photocatalytic reaction that contributes to better enhancing of the catalyst photoactivity performances and which is favorable to improve the efficiency of the water splitting process for HER.[21]

Long-time Photocatalytic HER stability

To study the long-term photocatalytic performance, a closed photoreactor system was used, where the pressure increase due to the production of hydrogen was continuously measured and recorded. **Figure SI 18** shows the pressure increasing in the reactor chamber together with their corresponding linear fit during the HER in which each catalyst is involved. Regarding gCN catalyst, the pressure increased very slightly within 48 hours of irradiation implying that the HER takes place very slowly within this time interval. This result also suggests that the loading process of Pt is hardly achievable when gCN is used as a catalyst meaning that the obtained catalytic system is not appropriate for highly efficient HER performances. After 48 hours of irradiation, the pressure increased barely up to 120 hours of irradiation. This means that for large-scale applications gCN cannot meet the needs when it comes to harvesting light to drive photocatalytic water splitting for HER.

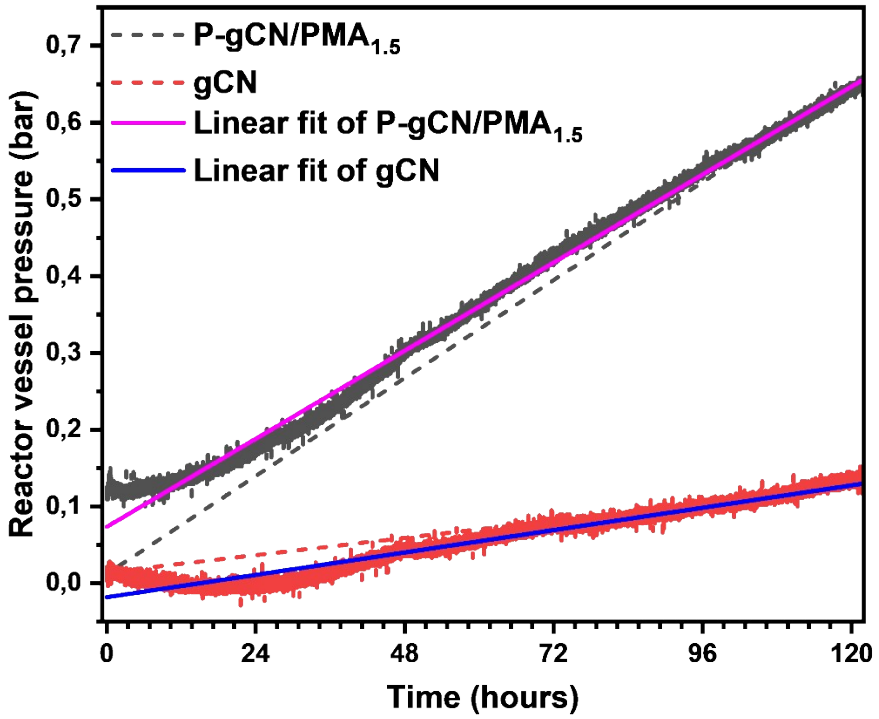

Figure SI 18: Long-time Photocatalytic HER

Regarding the slope of P-gCN/PMA$_{1.5}$ (**Figure 8b**), one can notice that only a few hours are required to complete the in-situ photo-deposition of Pt and allow the catalytic system ready to enhance efficiency HER performances. Then, a rapid increase of the pressure in the reactor chamber is observed with a very steep slope rising over 120 hours of irradiation (**Figure SI 18**). The hydrogen released corresponding to the pressure increase is shown in **Figure 8b**. The amount of hydrogen released is around 35 000 μmol.g-1 at 120 hours of irradiation and HER did not appear to be shut down at this stage. This observation helps to provide important information about P-gCN/PMA$_{1.5}$: This observation proves that the new electronic structure of P-gCN/PMA$_{1.5}$ is favorable for the efficient enhancement of in-situ Pt photo-deposition, which contributes to the achievement of an optimal catalytic system for improving the efficiency of light-driven HER. This observation also confirms the stability of the photoactivity and the improved lifetime of the photogenerated species. For many catalysts reported today, the photoactivity typically decreases after 48 or 72 hours of irradiation,[19] but for the P-gCN/PMA$_{1.5}$ synthesized in this work, the photoactivity is extremely pronounced and the catalyst can exhibit high HER performance for over 120 hours. This confirms also that the recombination process is extremely reduced and the lifetime of the photogenerated species (electrons and holes) is extremely prolonged, allowing for better light harvesting. Looking at the HER performance exhibited for over 120 hours, the as-prepared material could be used as a better candidate for large-scale application.

As depicted in **Figures SI 19 and SI 21a**, P-gCN/PMA$_{1.5}$ before and after the HER exhibits the same textural aspect, confirming its stability. In contrast with gCN, the textural aspect is not the same before and after the HER, implying its non-stability (**Figure SI 20 and SI 21b**).

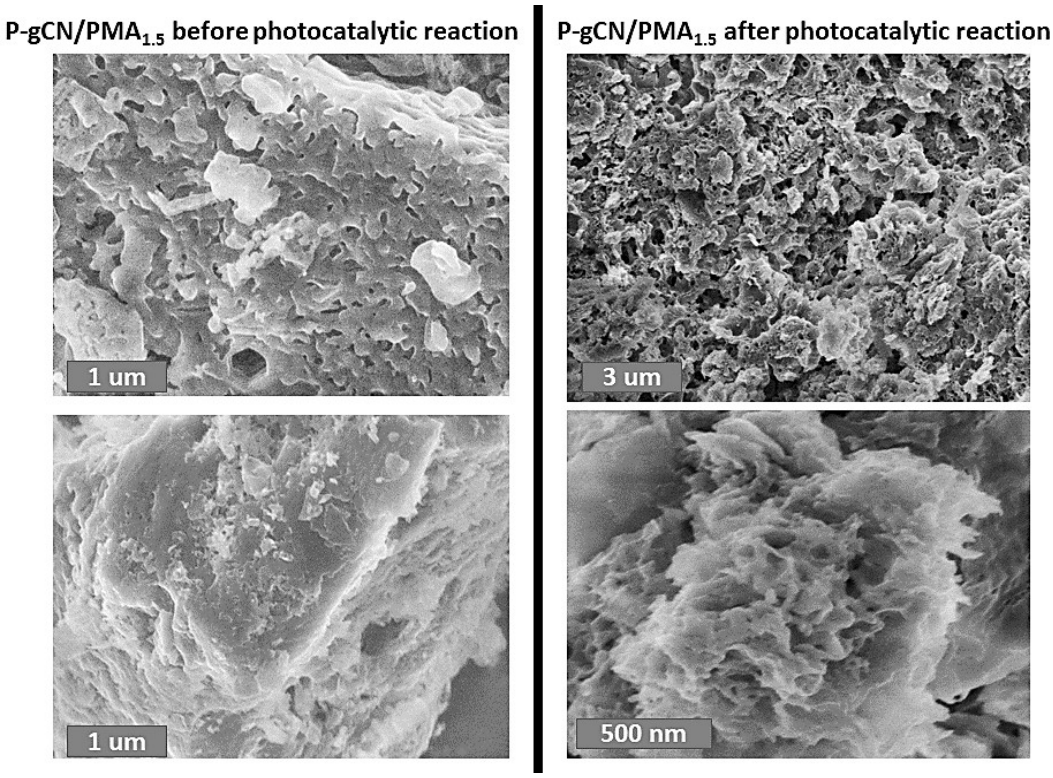

Figure SI 19: P-gCN/PMA$_{1.5}$ before and after the photocatalytic reaction

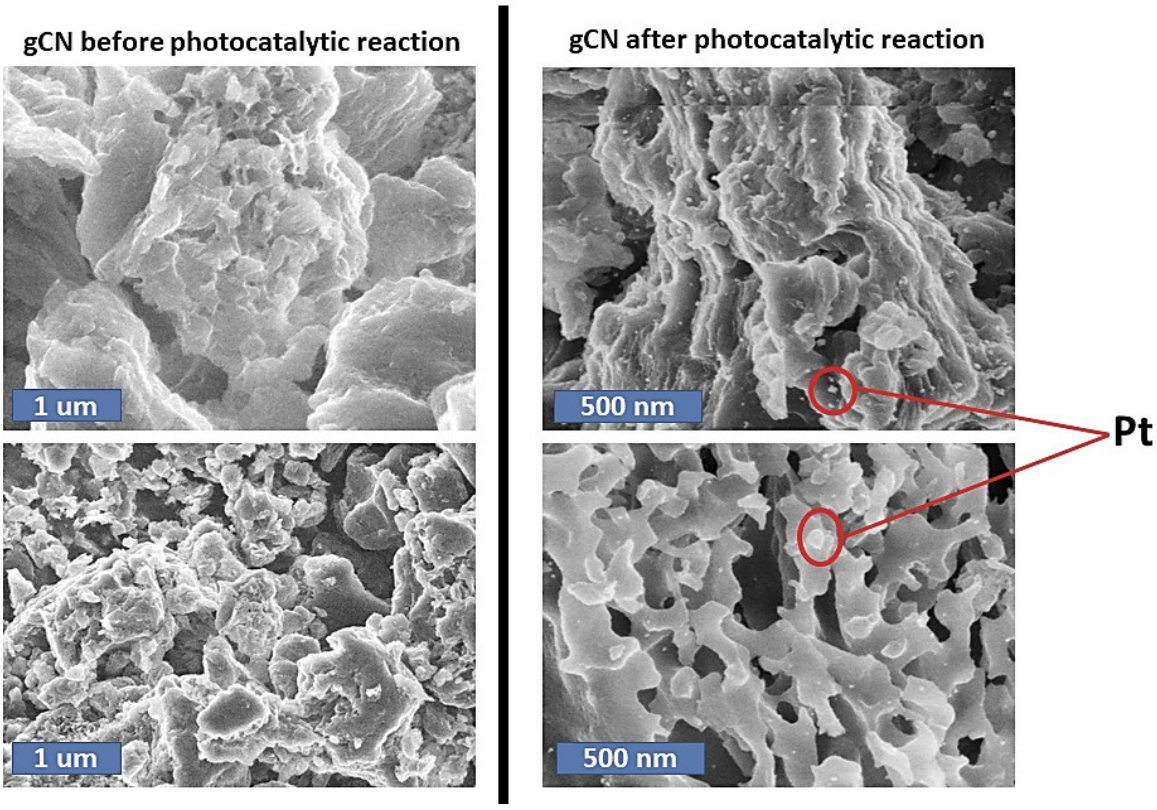

Figure SI 20: gCN before and after the photocatalytic reaction

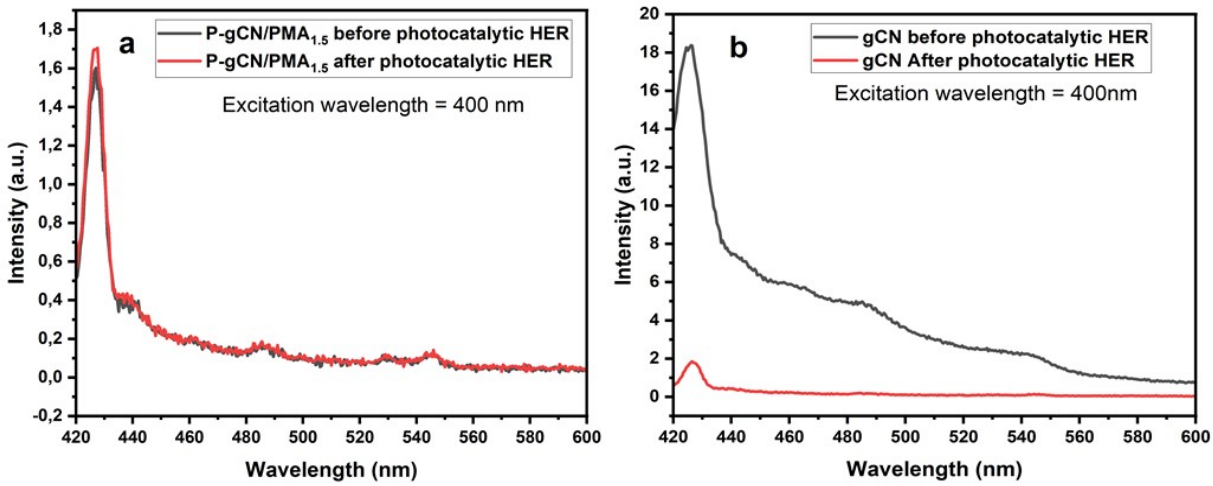

Figure SI 21: Photoluminescence (PL) spectra of P-gCN/$PMA_{1.5}$ (a) and gCN (b) with 400 nm excitation wavelength

P-gCN/$PMA_{1.5}$ towards overall water spitting

The final stage of our photocatalysis experiments was focused on the photocatalytic overall water splitting reaction. Some trial experiments to check whether the as-prepared catalyst can exhibit a successful response for hydrogen production through overall photocatalytic water splitting ,which means photocatalytic water splitting without any addition of the sacrificial agent (TEOA), were conducted. Thus, 10 mg of fresh P-gCN/$PMA_{1.5}$ catalyst was placed in the 35 mL reactor with 18 mL of water and 10 μL of Pt solution. After Ar degassing, the quartz reactor was placed under full spectrum light irradiation with an Xe arc lamp for 6 hours, 24 hours, and then for 120 hours separately. The same experiment was repeated with the recycled catalyst. The results of hydrogen evolution are recorded in **Table SI 4** according to each experimental condition. From the table below, one can notice that P-gCN/$PMA_{1.5}$ might certainly have evolved H_2 without the presence of a sacrificial agent. With a shorter irradiation time, very little amount of H_2 was detected from GC measurement at the end of the overall water-splitting reaction and about 6.4 μmol is emitted after 24 hours of irradiation. When the light irradiation is extended to 120 hours, no H_2 was detected by the GC measurement, which means that there is probably a strong back reaction in this water-splitting process (i.e. the recombination of hydrogen and oxygen to water) as these products are formed nearby.[25] Recycled P-gCN/$PMA_{1.5}$ enhanced H_2 evolution through photocatalytic overall water splitting reaction with an amount of 95.62 μmol of H_2 evolved after 24 hours of irradiation. Further research is required to provide a fundamental understanding of the experimental results. However, it is believed that by trying a series of metal cocatalysts with P-gCN/$PMA_{1.5}$, it is possible to provide a suitable catalytic system capable of enhancing H_2 evolution through the overall photocatalytic water splitting reaction.

Table SI 4: Operating conditions and H_2 evolution from overall water splitting

Catalysts	Mass (mg)	Light source	Irradiation time (hours)	H_2 (vol%)	H_2 evolved (μmol)
gCN	10	300 W Xe /full spectrum	6	ND	00
P-gCN/PMA$_{1.5}$	10	300 W Xe /full spectrum	6	0,005	3,5
P-gCN/PMA$_{1.5}$	10	300 W Xe /full spectrum	24	0,009	6,4
P-gCN/PMA$_{1.5}$	10	300 W Xe /full spectrum	120	ND	00
P-gCN/PMA$_{1.5}$ (Re)	10	300 W Xe /full spectrum	6	0,087	61,62
P-gCN/PMA$_{1.5}$ (Re)	10	300 W Xe /full spectrum	24	0,135	95,62

Re: recycled catalyst ND: Non-Detected

Apparent quantum efficiency (AQE)

The Apparent Quantum Efficiency AQE, also called AQY (Apparent Quantum Yield) generally refers to the efficiency of converting absorbed light into emitted light, which can be in the form of fluorescence[26,27]. In heterogeneous photocatalysis, quantum efficiency has come to define the number of reacted electrons relative to the total number of photons incident in the reaction system. For light-driven photocatalytic water splitting, the number of reacted electrons is assumed equivalent to the number of hydrogen produced, then the AQE characterizes the efficiency of hydrogen production performances in a photocatalytic reaction system[28,29]. The AQE measurements were performed under monochromatic LED light irradiation at a wavelength of 415 nm, and the light intensity was measured by an optical meter (ILT 2400). The photocatalytic reactions were carried out using the same conditions described at **SI 16**, except the light source was kept at about 1.5 to 2 cm from the reactor chamber and the diameter of the irradiation area was measured. Then for the H_2 yield of 3 h irradiation, the AQE was calculated by the following equation[28–30]:

$$AQE\% = \frac{2 \times N_{H_{2\,produced}}(mol)}{N_{incident\ photons}\,(mol)} \times 100$$

$$= \frac{[N_a \times h \times c] \times 2(N_{H_{2\,produced}})}{P \times S \times t \times \lambda} \times 100 \qquad (5)$$

Where N_a is the Avogadro's constant (6.022×10^{23} mol^{-1}), h is the Planck constant (6.626×10^{-34} J.s), c is the speed of light (3×10^{8} m.s^{-1}), s is the irradiation area on the reactor surface (cm^2), P is the power intensity of the incident light (W.cm^{-2}), t is the photoreaction time (s) and λ is the wavelength of the monochromatic light.

For the reaction involving sample P-gCN/PMA$_{1.5}$, the following parameters were recorded: H_2 (% vol) = 1.6, P = 28 mW.cm^{-2}, S= 3.14 cm^2. The calculated AQE is 0.7 %. For the reaction involving sample P-gCN/PMA$_{0.5}$, AQE of 0.3 % was obtained with the following parameters: H_2 (% vol) = 0.7, P = 28 mW.cm^{-2}, S= 3.14 cm^2. For the reaction involving sample gCN, AQE of 0.1 was obtained with the following parameters: H2 (% vol) = 1, P = 85 mW.cm^{-2}, S = 4.53 cm^2. Sample P-gCN/PMA$_{1.5}$ exhibits an AQE 7 times higher than the AQE exhibited by gCN, this confirms the boosting effect due to the PMA loaded onto the surface of gCN.

Section 4: Further catalyst characterization

Table SI 22: FWHM of XRD patterns disclosing the crystallinity

Samples	FWHM (rad) of XRD patterns
P-gCN/PMA$_{0.1}$	17.74
P-gCN/PMA$_{0.2}$	15.38
P-gCN/PMA$_{0.3}$	15.27
P-gCN/PMA$_{0.4}$	15.56
P-gCN/PMA$_{0.5}$	14.78
P-gCN/PMA$_{1}$	14.97
P-gCN/PMA$_{1.5}$	14.58
P-gCN/PMA$_{2}$	17.36
P-gCN/PMA$_{2.5}$	21.02
gCN	2.19

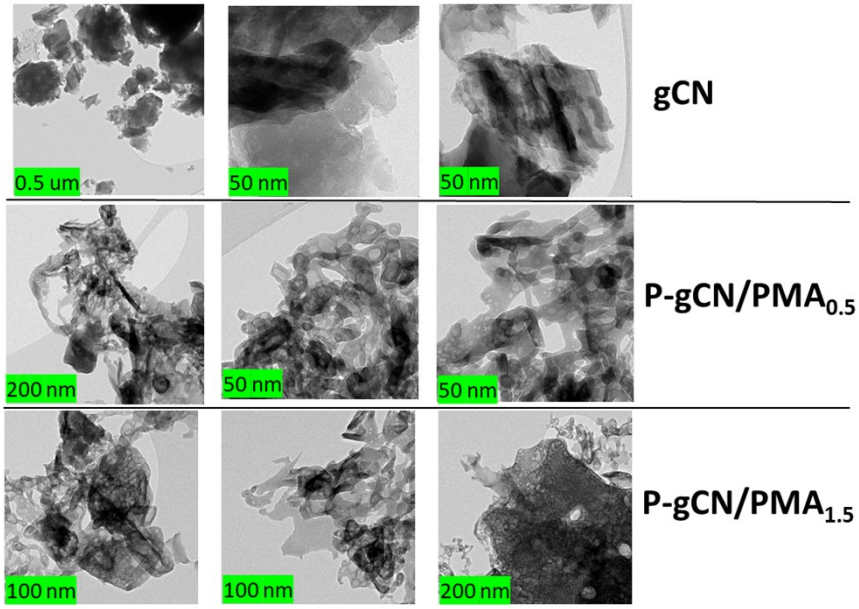

Figure SI 23: TEM images

Using the Gauss function through the Origin software, the Full Width at Half Maximum (FWHM) of each XRD pattern was estimated to predict the crystalline size following the Scherrer equation (**Table SI 22**). Despite gCN possessing the smallest FWHM from its XRD pattern which will result in the highest crystalline size, this sample exhibits a geometrical shape that is less defined and less oriented than other samples. This is observed by the TEM images displayed in **Figure SI 23** and confirmed by its SEM image (**Figure SI 2**). As compared to gCN, the loading of PMA during the solvothermal synthesis increases, of course, the FWHM of their corresponding XRD patterns in the final P-gCN/PMA_x material resulting in lower crystalline size but provides a well-defined 3D polymeric shape with a structure well oriented like nanorods. At lower concentration of PMA loaded (0.1 - 0.4 g), the XRD patterns of the corresponding P-gCN/PMA_x sample exhibits higher FWHM which means lower crystalline size but their geometrical shape and their regular arrangement is well defined making them more crystalized than gCN. At higher concentrations of PMA loaded (0.5 -1.5 g), the XRD patterns of the corresponding P-gCN/PMA_x sample exhibit lower FWHM which means higher crystalline size as compared to those samples with lower concentration of PMA loaded. In addition, those samples exhibit a well-defined shape and regular arrangement as compared to gCN and other samples. Sample P-gCN/$PMA_{0.5}$ has the best regular arrangement and the best stacking layers, it seems to possess higher crystallinity. At a saturated concentration of PMA (2 – 2.5 g), the crystalline size increases again.

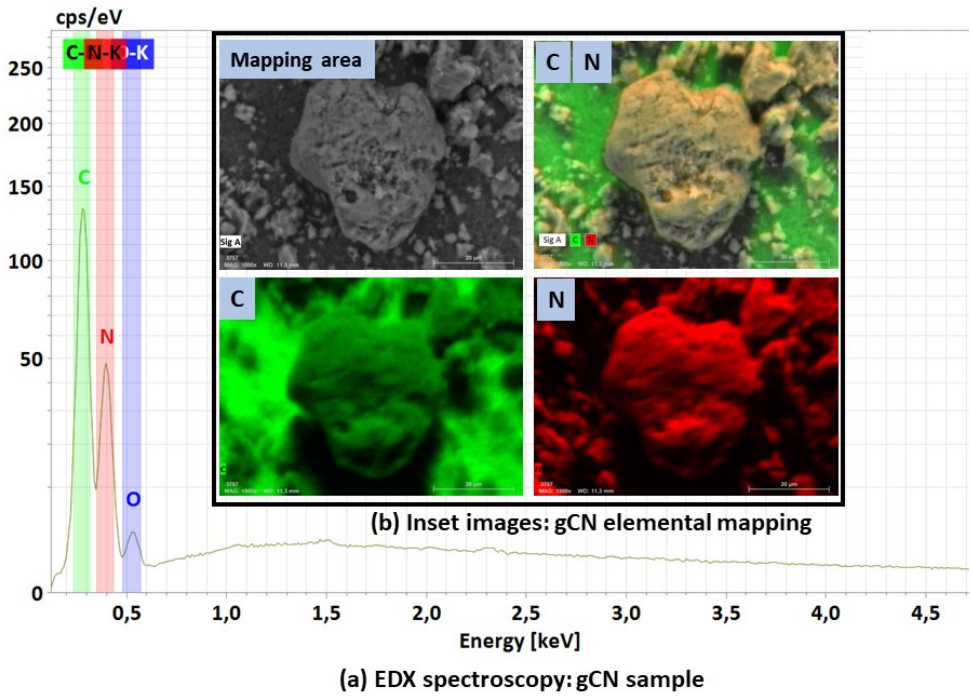

Figure SI 24: EDX spectroscopy (a) and elemental mapping (b) of gCN

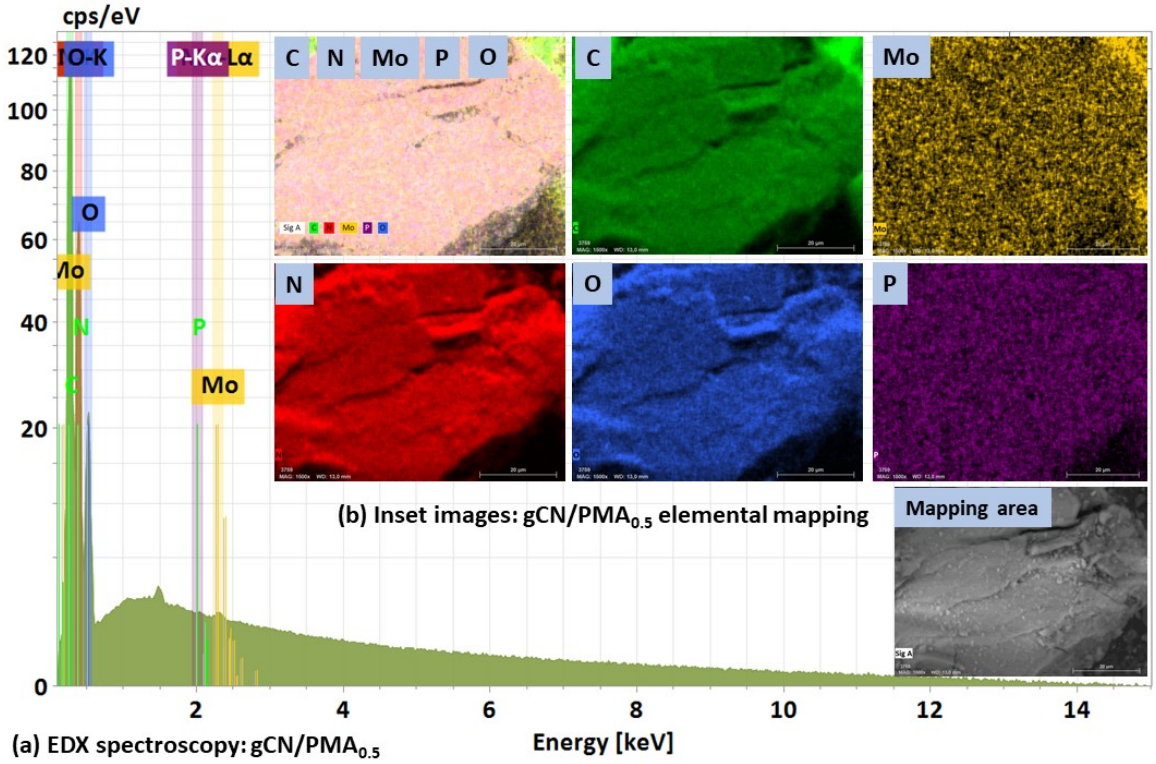

Figure SI 25: EDX spectroscopy (a) and elemental mapping (b) of bulk gCN/PMA$_{0.5}$

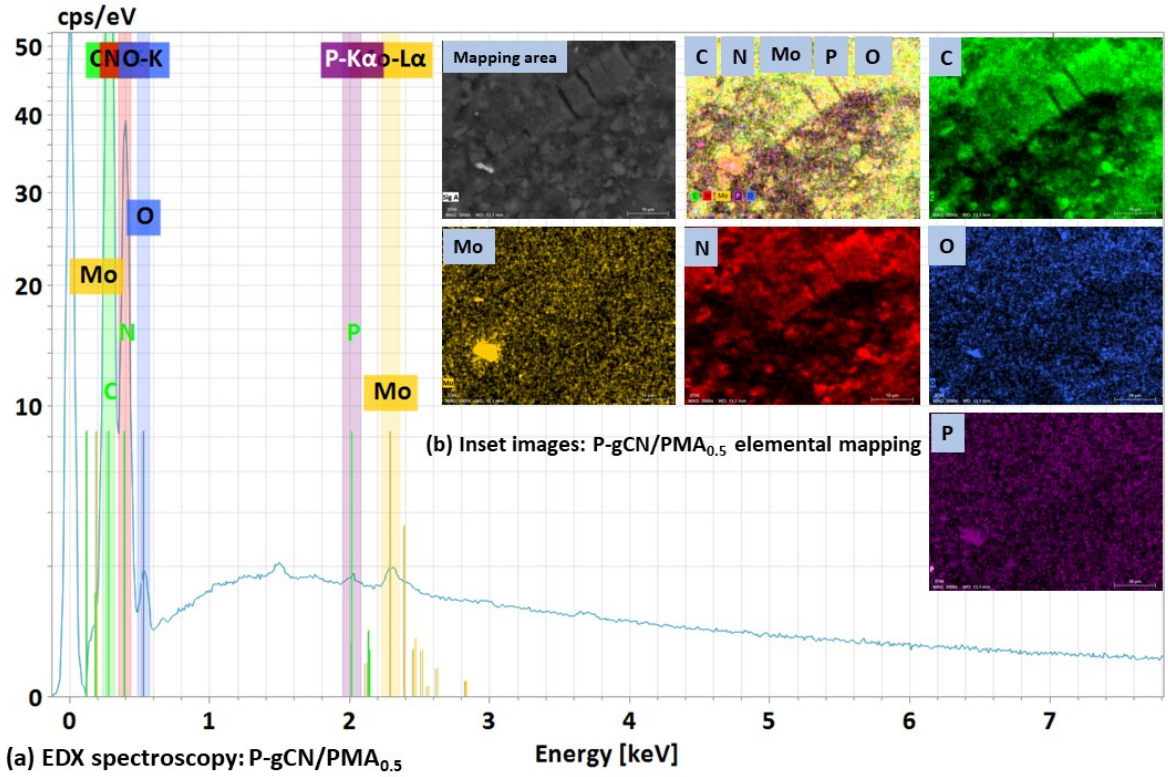

Figure SI 26: EDX spectroscopy (a) and elemental mapping (b) of P-gCN/PMA$_{0.5}$

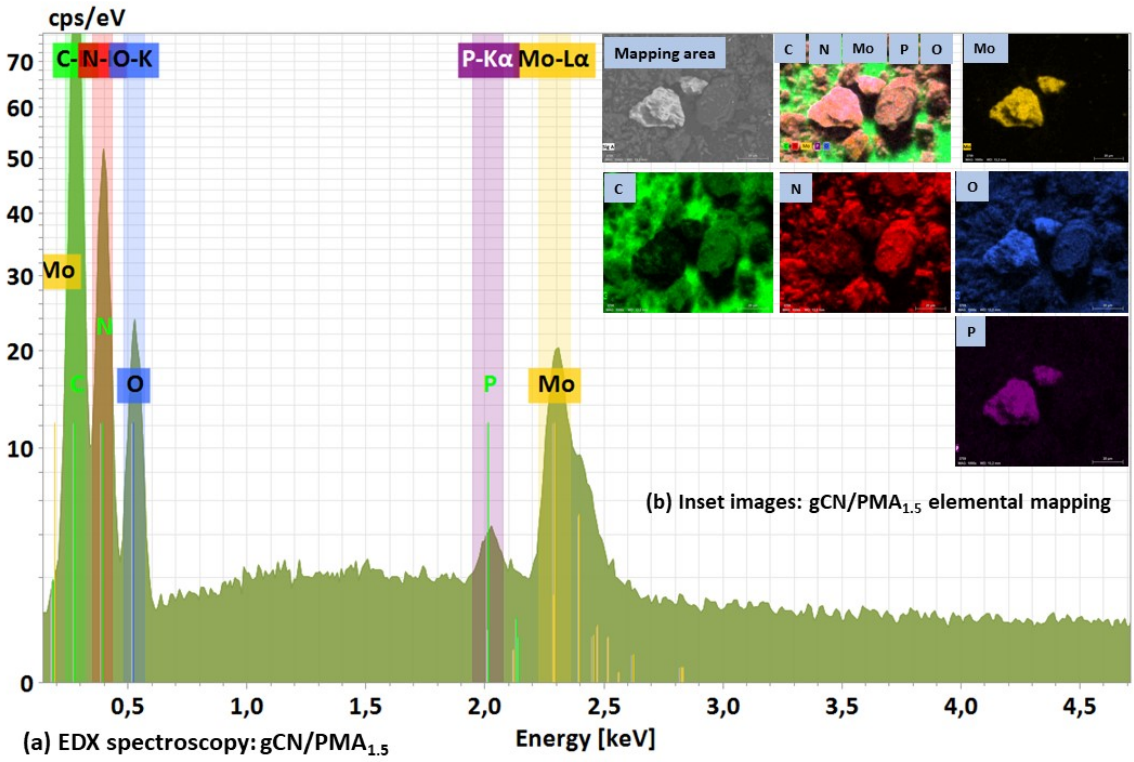

Figure SI 27: EDX spectroscopy (a) and elemental mapping (b) of bulk gCN/PMA$_{1.5}$

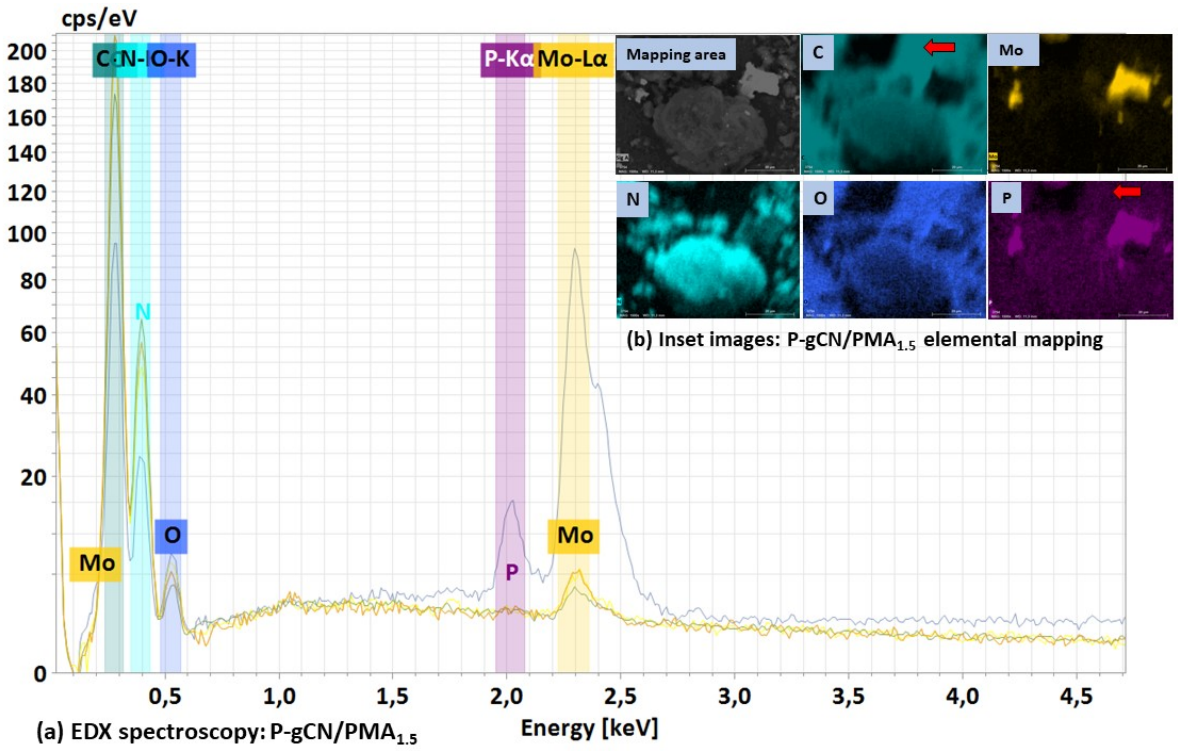

Figure SI 28: EDX spectroscopy (a) and elemental mapping (b) of P-gCN/PMA$_{1.5}$

To further elucidate the occurrence of P atoms, a look at the elemental mapping of the bulk materials gCN/PMA$_x$ (direct precursor of P-gCN/PMA$_x$) was taken. The elemental mapping and EDX spectroscopy (**Figures SI 25 and SI 27**) confirm that the corresponding bulk material contains

phosphorus throughout distributed into the gCN matrix. Furthermore, after post-annealing, it can be observed from the element mapping of P-gCN/PMA$_{0.5}$ and P-gCN/PMA$_{1.5}$ (**Figures SI 26 and SI 28**) that C, N, O, Mo, and P were distributed evenly throughout the entire skeleton of the heterostructure. The evidence of P-doping is agreed from the fact that P-atoms are distributed in the same area where C atoms are also distributed suggesting a replacement of some C atoms by some P atoms or suggesting that, electronic clouds from P atoms overlap electronic clouds of C atoms.

Table SI 29: Comparison of hydrogen evolution rates based on CN derivatives, number of catalyst components, and TEOA concentration

Catalysts	Number of components	Sacrificial agents TEOA (%)	H_2 evolution rate (umol.g^{-1}.h^{-1})	References
NiS/CdS/g-C_3N_4	3	20	3015	[31]
Holey ultrathin g-C_3N_4	1	12	2860	[32]
NiCo-MOF/ZIF	2	15	4170	[33]
Co@NC/g-C_3N_4-2	2	10	161	[34,35]
C_3N_4-Pd-Cu_2O	2	10	32.5	[35]
4NiL/CN	2	10	303.3	[36]
4Nil/NiOx/CN	3	10	524.1	[36]
Protonated Imine-linked COFs	2	10	20.7	[37]
W-TEOS-CN	3	10	326	[38]
W-SNP-CN	3	10	286	[38]
P-gCN/PMA$_{1.5}$	**2**	**10**	**625**	**This work**

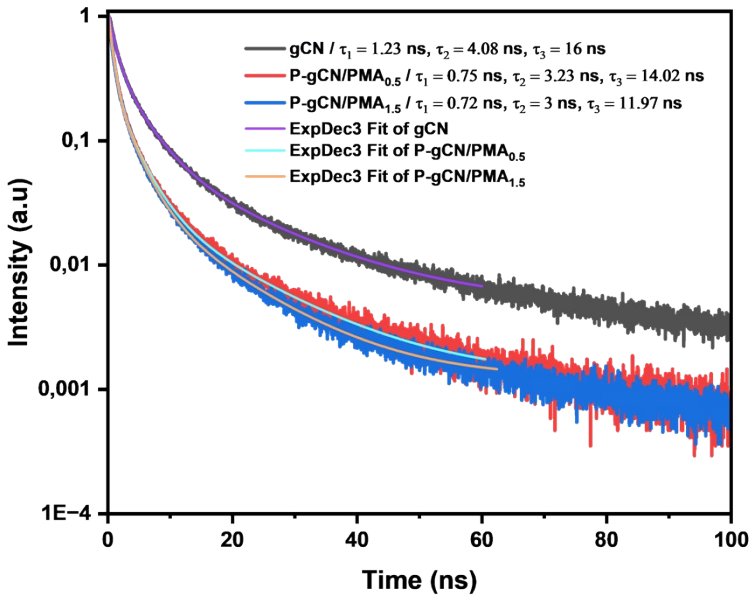

Figure SI 30: Comparison of time-resolved transient PL decay spectra of P-gCN/PMA$_{1.5}$ and P-gCN/PMA$_{0.5}$

Photocurrent measurements

gCN and P-gCN/PMA$_{1.5}$ samples were first immobilized on an FTO glass substrate to form their corresponding films which were used for PEC measurements with the use of a custom Teflon cell in a standard three-electrode system consisting of a reference (SCE) electrode (Ag/AgCl, XR300, sat. KCl, Radiometer Analytical), counter electrode (Pt wire), and working electrodes (FTO immobilized samples). EG&G Princeton Applied Research potentiostat (Model 273 A) coupled with a WACOM Class AAA solar simulator (AM1.5, 100 mW cm^{-2}) was used for these measurements. The electrolyte was 0.1 M KOH containing 5% TEOA buffer (KP$_i$, pH 7). The applied potential was converted to the RHE using the Nernst equation.

$$V_{RHE} = V_{Ag/AgCl} + (0.0591 \times pH) + V^{\circ}_{Ag/Cl} \qquad (6)$$

where V$_{Ag/AgCl}$ is the applied potential for the Ag/AgCl reference electrode and $V^{\circ}_{Ag/Cl}$ is the standard potential of the reference electrode (0.199 V). The cell is exposed to a solar irradiation source at regular time intervals to record photo-response. Based on the initial cyclic voltammetry experiments, chronoamperometry is performed to study the photo-response of samples. The films were immobilized by coating the corresponding precursor onto FTO glasses to obtain seed and followed by thermal annealing at 450 °C for 2 hours in alkoxide precursor solution in Argon atmosphere.

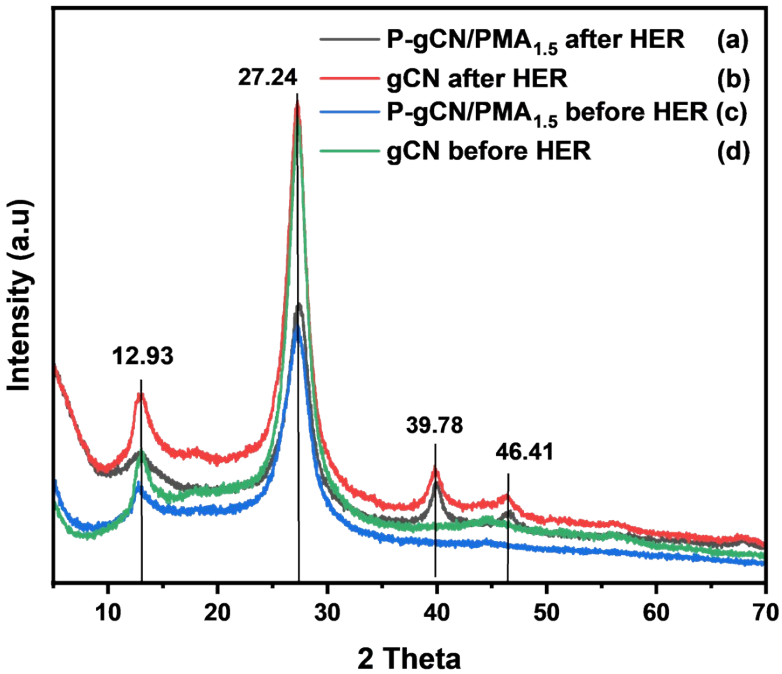

Figure SI 31: XRD patterns of gCN and P-gCN/PMA$_{1.5}$: After (a, b) and before (b, c) photocatalytic HER

Figure SI 31 supports additionally the stability of P-gCN/$PMA_{1.5}$. The diffraction peak at 2θ = 27.2° characteristic of gCN was equally exhibited in P-gCN/$PMA_{1.5}$ before and after the HER at almost similar intensity, confirming that the gCN backbone was kept as same in the lattice structure before and after the photocatalytic reaction. Only the peak at 2θ = 12.9° was exhibited in both situations at the same position but with different intensities, corresponding to Pt intercalation in the intra-layer (100) plane of gCN. The peaks at 2θ = 39.78° and 46.41° correspond to the face-centered cubic structure of platinum, demonstrating the presence of crystalline Pt (JCPDS Card 04-0802).[39] Except Pt diffraction peak which is part of the catalytic system, there is no new peak appeared and no new peak exhibited in XRD patterns after the HER, confirming that the catalyst is not destroyed and therefore, the stability of P-gCN/$PMA_{1.5}$ for photocatalytic water splitting reaction is demonstrated.

References

1 Q. Lin, L. Li, S. Liang, M. Liu, J. Bi and L. Wu, *Appl Catal B*, 2015, **163**, 135–142.

2 X. Wang, K. Maeda, A. Thomas, K. Takanabe, G. Xin, J. M. Carlsson, K. Domen and M. Antonietti, *Nat Mater*, 2009, **8**, 76–80.

3 S. Y. Tameu Djoko, H. Bashiri, E. T. Njoyim, M. Arabameri, S. Djepang, A. K. Tamo, S. Laminsi, M. Tasbihi, M. Schwarze and R. Schomäcker, *J Photochem Photobiol A Chem*, 2020, **398**, 112596.

4 L. Shi, F. Wang, Y. Wang, D. Wang, B. Zhao, L. Zhang, D. Zhao and D. Shen, *Sci Rep*, 2016, **6**, 21135.

5 V. Loddo, M. Bellardita, G. Camera-Roda, F. Parrino and L. Palmisano, *Heterogeneous Photocatalysis: A Promising Advanced Oxidation Process*, Elsevier Inc., 2018.

6 G. Marcì, E. I. García-Lõpez and L. Palmisano, *Eur J Inorg Chem*, 2014, 21–35.

7 N. Al-zaqri, A. Alsalme, S. F. Adil, A. Alsaleh, S. G. Alshammari, S. I. Alresayes, R. Alotaibi, M. Al-Kinany and M. R. H. Siddiqui, *Journal of Saudi Chemical Society*, 2017, **21**, 965–973.

8 K. N. Rao, R. Gopinath, A. Hussain, N. Lingaiah and P. S. S. Prasad, *Influence of ammonium salt formation on the activity and selectivity of the 12-molybdophosphate heteropolyacid catalyst prepared by solid-solid interaction in the ammoxidation of 2-methylpyrazine*, 2000, vol. 68.

9 K. N. Rao, N. Lingaiah, I. Suryanarayana and P. S. S. Prasad, *A comparison of structure and catalytic functionality of 12-molybdophosphoric acid and its ammonium salt in the ammoxidation of 2-methylpyrazine to 2-cyanopyrazine Ã*, 2003, **90**, 1-2.

10 L. Jiang, X. Yuan, Y. Pan, J. Liang, G. Zeng, Z. Wu and H. Wang, *Appl Catal B*, 2017, **217**, 388–406.

11 Y. Feng, S. Lin, S. Huang, S. Shrestha and G. Conibeer, *J Appl Phys*, 2015, **117**, 125701.

12 K. A. Ali, A. Z. Abdullah and A. R. Mohamed, *Appl Catal A Gen*, 2017, **537**, 111–120.

13 X. Kang, Y. Kang, X. Hong, Z. Sun, C. Zhen, C. Hu, G. Liu, and H. Cheng, *Progress in Natural Science: Materials International*, 2018, **28**, 183–188.

14 B. J. Ng, L. K. Putri, X. Y. Kong, Y. W. Teh, P. Pasbakhsh and S. P. Chai, *Advanced Science*, 2020, **7**.

15 J. Fu, J. Yu, C. Jiang and B. Cheng, *Adv Energy Mater*, 2018, **8**.

16 *H. Kent Baker, John R. Nofsinger. Socially Responsible Finance and Investing. John Wiley & Sons, Inc. USA, 2012, 1-66.*

17 V. Balzani, A. Credi and M. Venturi, *ChemSusChem*, 2008, 1, 26–58.

18 S. B. Agrawal, S. Singh and M. Agrawal, *INTERNATIONAL JOURNAL OF PLANT AND ENVIRONMENT*, 2015, **1**, 43–56.

19 J. ying Tang, D. Yang, W. guo Zhou, R. tang Guo, W. guo Pan and C. ying Huang, *J Catal*, 2019, **370**, 79–87.

20 W. J. Chun, A. Ishikawa, H. Fujisawa, T. Takata, J. N. Kondo, M. Hara, M. Kawai, Y. Matsumoto and K. Domen, *Journal of Physical Chemistry B*, 2003, **107**, 1798–1803.

21 B. N. Popov, in *Corrosion Engineering*, Elsevier, 2015, pp. 29–92.

22 N. Iqbal, A. Afzal, I. Khan, M. S. Khan and A. Qurashi, *Sci Rep*, 2021, **11**, 16886.

23 Z. Huang, J. Liu, S. Zong, X. Wang, K. Chen, L. Liu and Y. Fang, *J Colloid Interface Sci*, 2022, **606**, 848–859.

24 Y. W. Chen and Y. H. Hsu, *Catalysts*, 2021, **11**, 966.

25 B. Mei, K. Han and G. Mul, *ACS Catal*, 2018, **8**, 9154–9164.

26 R. Li and C. Li, in *Advances in Catalysis*, Academic Press Inc., 2017, vol. **60**, pp. 1–57.

27 S. Sadjadi, in *Emerging Carbon Materials for Catalysis*, Elsevier, 2020, pp. 123–160.

28 J. Yang, S. Ghosh, J. Roeser, A. Acharjya, C. Penschke, Y. Tsutsui, J. Rabeah, T. Wang, S. Y. Djoko Tameu, M. Y. Ye, J. Grüneberg, S. Li, C. Li, R. Schomäcker, R. Van De Krol, S. Seki, P. Saalfrank and A. Thomas, *Nat Commun*, , 2022, **13**, 6317.

29 J. Huang, X. Li, X. Jin, L. Wang, Y. Deng, F. Su, P. K. Wong and L. Ye, *Mater Adv*, 2020, **1**, 363–370.

30 L. Liu, M.-Y. Gao, H. Yang, X. Wang, X. Li, and A. I. Cooper, *JACS*, 2021, **143**, 19287-19293.

31 X. Wang, H. Jiang, M. Zhu, and X. Shi, *Chinese Chemical Letters*, 2023, **34**, 107683.

32 Y. Li, R. Jin, Y. Xing, J. Li, S. Song, X. Liu, M. Li, and R. Jin, *Adv Energy Mater*, 2016, 1601273.

33 T. Li, Y. Li, and Z. Jin, *Inorg Chem*, 2022, **61**, 12809–12821.

34 Y. Li, S. Zhu, X. Kong, Y. Liang, Z. Li, S. Wu, C. Chang, S. Luo and Z. Cui, *Environ Res*, 2021, **197**, 111002.

35 W. Yin, L. Bai, Y. Zhu, S. Zhong, L. Zhao, Z. Li and S. Bai, *ACS Appl Mater Interfaces*, 2016, **8**, 23133–23142.

36 Y. X. Zhang, S. Tang, W. De Zhang and Y. X. Yu, *ACS Appl Mater Interfaces*, 2019, **11**, 14986–14996.

37 J. Yang, A. Acharjya, M. Y. Ye, J. Rabeah, S. Li, Z. Kochovski, S. Youk, J. Roeser, J. Grüneberg, C. Penschke, M. Schwarze, T. Wang, Y. Lu, R. van de Krol, M. Oschatz, R. Schomäcker, P. Saalfrank and A. Thomas, *Angewandte Chemie - International Edition*, 2021, **60**, 19797–19803.

38 K. Kailasam, A. Fischer, G. Zhang, J. Zhang, M. Schwarze, M. Schröder, X. Wang, R. Schomäcker and A. Thomas, *ChemSusChem*, 2015, **8**, 1404–1410.

39 M. A. Shah, *Scientia Iranica*, 2012, **19**, 964–966.